bioRxiv preprint doi: https://doi.org/10.1101/016733; this version posted March 19, 2015. The copyright holder for this preprint (which was not certified by peer review) is the author/funder, who has granted bioRxiv a license to display the preprint in perpetuity. It is made available under aCC-BY 4.0 International license.

Mapping the Conformational Landscape of a Dynamic Enzyme by XFEL and Multitemperature Crystallography

Daniel A. Keedy[1*], Lillian R. Kenner[1*], Matthew Warkentin[2*], Rahel A. Woldeyes[1*], Michael C. Thompson[1], Aaron S. Brewster[3], Andrew H. Van Benschoten[1], Elizabeth L. Baxter[4], Jesse B. Hopkins[2], Monarin Uervirojnangkoorn[5,6], Scott E. McPhillips[4], Jinhu Song[4], Roberto Alonso-Mori[7], James M. Holton[3,4,8], William I. Weis[5,9,10], Axel T. Brunger[5,6,9,10], S. Michael Soltis[4], Henrik Lemke[7], Ana Gonzalez[4], Nicholas K. Sauter[3], Aina E. Cohen[4], Henry van den Bedem[4#], Robert E. Thorne[2#], James S. Fraser[1#]

1 - Dept. of Bioengineering and Therapeutic Sciences, University of California, San Francisco, San Francisco, CA 94158
2 - Physics Dept., Cornell University, Ithaca, NY 14853
3 - Physical Biosciences Division, Lawrence Berkeley National Laboratory, Berkeley, CA 94720
4 - Stanford Synchrotron Radiation Lightsource, SLAC National Accelerator Laboratory, Menlo Park, CA 94025
5 - Dept. of Molecular and Cellular Physiology, Stanford University, Stanford, CA 94305
6 - Howard Hughes Medical Institute, Stanford University, Stanford, CA 94305
7 - Linac Coherent Light Source, SLAC National Accelerator Laboratory, Menlo Park, CA 94025
8 - Dept. of Biochemistry and Biophysics, University of California, San Francisco, San Francisco, CA 94158
9 - Dept. of Structural Biology, Stanford University, Stanford, CA 94305
10 - Dept. of Photon Sciences, SLAC National Accelerator Laboratory, Menlo Park, CA 94025

Author contributions:

Prepared Samples: LRK, MW, JSF
Collected XFEL Data: LRK, RAW, ASB, AHVB, ELB, SEM, JS, RAM, SMS, HL, AG, AEC, HvdB, JSF
Collected Synchrotron data: MW, JBH, HvdB, JSF
Processed Data: RAW, ASB, NKS, MCT, AHVB, DAK, MU, JMH, WIW, ATB, AG
Analyzed Data: DAK, RAW, MCT, HvdB, JSF
Wrote Paper: DAK, RAW, HvdB, RET, JSF
Edited Paper: All authors

*equal contributions
#corresponding authors: vdbedem@slac.stanford.edu, ret6@cornell.edu, james.fraser@ucsf.edu

Abstract

Determining the interconverting conformations of dynamic proteins in atomic detail is a major challenge for structural biology. Conformational heterogeneity in the active site of the dynamic enzyme cyclophilin A (CypA) has been previously linked to its catalytic function. Here we compare the conformational ensembles of CypA by fixed-target X-ray free electron laser (XFEL) crystallography and multitemperature synchrotron crystallography. The "diffraction-before-destruction" nature of XFEL experiments provides a radiation-damage-free view of the functionally important alternative conformations of CypA. We monitored the temperature dependences of these alternative conformations with eight synchrotron datasets spanning 100-310 K. Multiconformer models show that many alternative conformations in CypA are populated above, but not below, the glass transition temperature (~200 K) and reveal abrupt changes in protein flexibility that provide all-atom insight into conformational coupling. Together, our XFEL data and multitemperature analyses motivate a new generation of time-resolved experiments to structurally characterize the dynamic underpinnings of protein function.

bioRxiv preprint doi: https://doi.org/10.1101/016733; this version posted March 19, 2015. The copyright holder for this preprint (which was not certified by peer review) is the author/funder, who has granted bioRxiv a license to display the preprint in perpetuity. It is made available under aCC-BY 4.0 International license.

Introduction

Current structural biology methods provide only incomplete pictures of how proteins can interconvert between distinct conformations (Motlagh et al., 2014; van den Bedem and Fraser, 2015). X-ray crystallography reveals atomic coordinates with relatively high accuracy and precision. However, because X-ray diffraction is an ensemble experiment involving greater than millions of copies of the protein in one crystal, the resulting electron density maps may contain contributions from multiple alternative conformations (Rejto and Freer, 1996; Smith et al., 1986; Woldeyes et al., 2014). At high resolution, it is often possible to detect and discretely model these alternative conformations (Burnley et al., 2012; Davis et al., 2006; Lang et al., 2010; van den Bedem et al., 2009). Structural characterization of alternative conformations by X-ray crystallography can complement NMR (Baldwin and Kay, 2009; Fenwick et al., 2014) and computational simulations (Dror et al., 2012; Ollikainen et al., 2013) in defining the role of protein dynamics in function (Henzler-Wildman and Kern, 2007).

Unfortunately, X-ray-induced radiation damage can complicate the interpretation of electron density maps (Garman, 2010; Holton, 2009; Warkentin et al., 2013). As a result, more than 95% of crystal structures are determined at cryogenic conditions (~100 K) to minimize diffusion of reactive intermediates and any subsequent structural relaxations (Garman, 2010). Although cryocooling minimizes radiation damage per unit X-ray dose, it can also modify mainchain and sidechain conformational distributions, particularly near active sites and in distal regions important for allosteric function (Fraser et al., 2011; Halle, 2004; Keedy et al., 2014). Recent studies have instead used a combination of room-temperature data collection and new computational tools to reveal a multitude of previously "hidden" alternative conformations, many of which can be directly linked to function (Deis et al., 2014; Fraser et al., 2009; Fukuda and Inoue, 2015; Keedy et al., 2014; van den Bedem et al., 2013). For example, the interconversion between alternative conformations revealed by room-temperature crystallography in the active site of the proline isomerase cyclophilin A (CypA) is rate-limiting for catalysis (Fraser et al., 2009). However, radiation damage considerations limit the applicability of room-temperature crystallography only to systems that yield large and well-diffracting crystals (Holton and Frankel, 2010; Warkentin et al., 2014; Zeldin et al., 2013). To visualize the mechanisms by which perturbations such as ligand binding, mutation, and temperature shift the relative populations of alternative conformations, new technologies are needed to break the connection between radiation damage and diffraction resolution.

Fortunately, the advent of X-ray free electron lasers breaks this connection and expands our ability to observe conformational heterogeneity at room temperature while avoiding radiation damage (Kern et al., 2014; Spence et al., 2012). XFELs deliver ultra-bright X-ray pulses, thereby allowing strong diffraction at a faster timescale than conventional radiation damage processes can occur (Neutze et al., 2000). This "diffraction-before-destruction" approach has been successful with two primary experimental configurations. In serial femtosecond crystallography (SFX), datasets are comprised of single exposures from thousands of individual nanocrystals injected from a slurry into the X-ray beam (Boutet et al., 2012; Liu et al., 2013). Room temperature SFX results

bioRxiv preprint doi: https://doi.org/10.1101/016733; this version posted March 19, 2015. The copyright holder for this preprint (which was not certified by peer review) is the author/funder, who has granted bioRxiv a license to display the preprint in perpetuity. It is made available under aCC-BY 4.0 International license.

have revealed important conformational differences compared to the cryogenic synchrotron structure of the human serotonin receptor GPCR (Liu et al., 2013). The SFX technique has potential applications for monitoring irreversible reactions and overcoming additional technical limitations inherent to Laue crystallography at synchrotrons (Neutze and Moffat, 2012). By contrast, in serial femtosecond rotation crystallography (SF-ROX), datasets are comprised of multiple exposures from each of dozens of individual macrocrystals mounted on fixed-target goniometers (Cohen et al., 2014; Hirata et al., 2014; Suga et al., 2015). This technique more closely mirrors existing protocols at synchrotrons. However, because both the crystal is effectively stationary during data collection in both types of XFEL experiments only partial intensity measurements are recorded. In SFX this problem is overcome by massive redundancy and Monte Carlo integration (White et al., 2013). Previous SF-ROX experiments carefully rotated the crystal between shots in steps that are finer than the mosiacity, which necessitates long crystals to accurately measure most reflections. However, recent advances in post-refinement can significantly reduce the number of images required for a complete dataset (Uervirojnangkoorn et al., 2015). Additionally, previous SF-ROX experiments have used cryocooled macrocrystals, which counteracts many of the advantages of XFEL crystallography and forgoes opportunities for time-resolved experiments.

Although time-resolved experiments are a particularly promising direction for XFEL crystallography, they require a trigger to rapidly initiate the conformational change (Neutze and Moffat, 2012; Spence et al., 2012). For example, time-resolved studies using laser excitation of the naturally occurring chromophore in PYP have yielded temporally resolved structural changes (Tenboer et al., 2014). Because light-responsive chemical triggers that initiate the conformational changes are often system-specific, more general approaches are needed to observe how protein conformational ensembles respond to perturbations as a function of time (Trincao et al., 2013). Temperature is a promising and generalizable candidate perturbation because it modulates protein conformational distributions (Fraser et al., 2011), and rapid temperature jumps can likely be triggered in crystals by laser-induced Raman excitation of the water in the solvent channels (Moffat, 1989). While time-dependent temperature perturbations have not been measured in protein crystals, classic work has examined the equilibrium temperature dependence of protein flexibility across individual structures determined at temperatures from ~80-320 K (Frauenfelder et al., 1987; Frauenfelder et al., 1979; Tilton et al., 1992). By using refined atomic B-factors as a proxy for flexibility, these studies identified a dramatic collective inflection point around 180-220 K (Frauenfelder et al., 1987; Tilton et al., 1992); however, the molecular origins of this “glass transition” remain incompletely understood and NMR studies indicate that distinct bands of motion have heterogeneous responses to temperature around the glass transition (Lee and Wand, 2001). An all-atom, multiconformer analysis of electron density maps at multiple temperatures could define whether there are collective shifts in the distributions of conformational substates and also set the stage for time-resolved structural experiments to define the rates and pathways of transitions between them.

bioRxiv preprint doi: https://doi.org/10.1101/016733; this version posted March 19, 2015. The copyright holder for this preprint (which was not certified by peer review) is the author/funder, who has granted bioRxiv a license to display the preprint in perpetuity. It is made available under aCC-BY 4.0 International license.

Here, we combine room-temperature fixed-target XFEL and multitemperature synchrotron experiments to examine the temperature-dependent conformational heterogeneity of the model enzyme CypA. First, we map the conformational distribution revealed at room temperature in the absence of radiation damage by XFEL SF-ROX diffraction using only 1,239 diffraction images and post-refinement using *prime* (Uervirojnangkoorn et al., 2015). This XFEL data validates previous connections between alternative conformations imaged in the crystal and experiments performed in solution (Eisenmesser et al., 2005; Fraser et al., 2009). Next we measured the equilibrium conformational ensemble across a broad range of temperatures, revealing complex and abrupt changes as a function of temperature. Our work uncovers a heterogeneous temperature dependence of functional alternative protein conformations and suggests new ways to use XFEL crystallography to probe the dynamic underpinnings of protein function. These new XFEL capabilities will allow us to probe a wide range of radiation-damage-sensitive systems that are otherwise intractable for conventional room-temperature diffraction at synchrotrons.

Results

Fixed-Target Collection Using XFELs Reveals Radiation-Damage-Free Conformational Heterogeneity

To compare the distribution of alternative conformations between XFEL and synchrotron diffraction data, we collected two ambient temperature datasets: a 1.75 Å resolution radiation-damage-free dataset using serial femtosecond rotation crystallography (SF-ROX) (Hirata et al., 2014; Schlichting, 2015; Suga et al., 2015) and a new 1.2 Å resolution synchrotron dataset. For the XFEL experiment, we collected 1,239 individual frames, translating to unique unexposed regions of 71 crystals between each shot (**Movie 1**), and processed the data using *cctbx.xfel* (Hattne et al., 2014). Post-refinement in *prime* was essential for extracting a dataset with high completeness using the limited amount of images that can be recorded during short screening shifts at the LCLS (Uervirojnangkoorn et al., 2015). Automated molecular replacement yielded interpretable electron density maps that allowed us to refine a single-conformer structural model with reasonable statistics (**Table 1**).

In agreement with our previous room-temperature and solution studies (Fraser et al., 2009), the XFEL and synchrotron mFo-DFc difference maps reveal evidence for catalytically-essential alternative conformations extending from the active site into the core of the protein (**Figure 1A,B**). For example, the rotamer jump of Phe113, which is coupled to a backbone adjustment exemplifying the backrub motion (Davis et al., 2006; Ollikainen et al., 2013), is apparent from a large positive mFo-DFc peak in both maps, which can be well modeled by a multiconformer model (**Figure 1C,D**). Next, we performed automated electron-density scanning using Ringer (Lang et al., 2014; Lang et al., 2010), which identifies alternative conformations at low levels of electron density by evaluating the density value at each potential position for the γ atom about the $\chi 1$ dihedral angle. We focused on two residues, Ser99 and Leu98, which are key markers of the conformational exchange by NMR (Eisenmesser et al., 2002; Eisenmesser et al., 2005) and were implicated in our previous room-temperature X-ray

bioRxiv preprint doi: https://doi.org/10.1101/016733; this version posted March 19, 2015. The copyright holder for this preprint (which was not certified by peer review) is the author/funder, who has granted bioRxiv a license to display the preprint in perpetuity. It is made available under aCC-BY 4.0 International license.

and mutagenesis experiments (Fraser et al., 2009). Despite the lower resolution of the XFEL dataset, Ringer sampling revealed evidence for alternative conformations observed in the synchrotron dataset for core residue Ser99 (**Figure 1E**). We did not conclusively observe a peak for a discrete alternative conformation of Leu98 (**Figure 1F**), but that is likely due to the lower resolution of the XFEL dataset. However, the asymmetric Ringer profile and the shift in the peak towards 300° indicate that the heterogeneity of Leu98 might be sufficiently modeled by the B-factors in the XFEL model.

To interpret difference-map features and Ringer peaks, we built multiconformer models for both datasets using *qFit* (van den Bedem et al., 2013; van den Bedem et al., 2009) and then finalized the models with *phenix.refine* and manual adjustments of alternative conformations (Adams et al., 2010) (**Figure 1C,D**, **Table 2**). The final models feature alternative conformations across the active-site network and are strongly supported by 2mFo-DFc electron density. Because of the lower resolution of the XFEL dataset, we were unable to definitively resolve the Leu98 alternative conformation and the partial-occupancy water overlaying the Phe113 alternative conformations; however, there is strong evidence for the other alternative conformations in the active-site network. These results indicate that XFEL crystallography can reveal native alternative conformations at high resolution and confirm that the alternative conformations observed in the synchrotron dataset are not an artifact of radiation damage. The observation of functionally important alternative conformations in CypA using fixed-target XFEL experiments further suggests that this approach can be expanded to studying the functional importance of conformational heterogeneity for other systems that are presently intractable for room-temperature diffraction at synchrotrons due to radiation damage.

Multitemperature X-ray Datasets Reveal Perturbed Conformational Ensembles of CypA

To probe the conformational landscape of CypA revealed by the room-temperature XFEL and synchrotron datasets, we collected eight high-resolution (1.34-1.58 Å) synchrotron crystallographic datasets across a wide range of temperatures from 100-310 K (**Table 1**). For each dataset, we initially refined single-conformer models. Although the single-conformer models are very similar to each other, the accompanying electron density maps reveal differences throughout the protein. In the active-site network, the mFo-DFc difference electron density maps are relatively featureless below 200 K, suggesting that a single conformation is a valid fit below this temperature. In contrast, positive and negative mFo-DFc peaks become gradually more prevalent as temperature increases above 200 K, suggesting that multiple conformations are increasingly required to explain the data as temperature increases (**Figure 3 - S1**).

We quantified the shift from single-conformation to multiple conformations with visual (**Figure 2A,B**) and statistical (**Figure 2C,D**) Ringer analysis. For both Ser99 (**Figure 2A**) and Leu98 (**Figure 2B**), a single peak is evident at all temperatures. The reduced height of these peaks as temperature increases is accompanied by the increase in a secondary peak for the minor conformation. This shift is most notable above 200 K, which

bioRxiv preprint doi: https://doi.org/10.1101/016733; this version posted March 19, 2015. The copyright holder for this preprint (which was not certified by peer review) is the author/funder, who has granted bioRxiv a license to display the preprint in perpetuity. It is made available under aCC-BY 4.0 International license.

corresponds to the glass transition temperature previously identified in protein crystals (Ringe and Petsko, 2003). To quantify this trend, we computed correlation coefficients between all pairs of Ringer curves for each residue (**Figure 2C,D**). Pairs of curves for similar temperatures have higher correlations than those for different temperatures. In particular, correlations for pairs of curves from temperatures that span the 200 K threshold are much lower than from temperatures that are both <200 K or both >200 K, emphasizing the changes in conformational heterogeneity that occur across the glass transition.

To ground this conformational redistribution in all-atom detail, we built a multiconformer model with *qFit* (van den Bedem et al., 2013; van den Bedem et al., 2009) for each multitemperature dataset. As with the room-temperature synchrotron and XFEL models, the finalized multiconformer models were improved over the single-conformer models (**Table 2**). Below the ~200 K glass transition temperature, the active-site network is best modeled as a single state, with ordered water molecules clearly evident adjacent to Phe113 (**Figure 3**, top row). Above 200 K, by contrast, multiple conformations provide a better explanation of the data. Interestingly, some partial-occupancy water molecules still co-occur with the major conformations (**Figure 3**, middle and bottom rows; **Movie 2**). Met61 appears to populate additional conformations above the glass transition, although it is difficult to precisely define changes in its conformational ensemble as temperature increases (see Methods). This residue bridges Phe113 and the catalytic Arg55 via steric contacts between alternative conformations in both directions, emphasizing the importance of modeling multiple conformations in all-atom detail for understanding inter-residue coupling. More generally, our multiconformer models separate harmonic from non-harmonic contributions to flexibility, which was a significant limitation of previous studies of the glass transition that relied on B-factors in single-conformer models (Frauenfelder et al., 1987; Tilton et al., 1992).

Some Regions Feature Conformational Heterogeneity Only Below the Glass Transition Temperature

Although more conformational heterogeneity is evident at higher temperatures in the active site of CypA, theoretical studies suggest the counterintuitive idea that some additional conformations can be accessed only as temperature decreases (Halle, 2004). We observed that one region of CypA exhibits backbone alternative conformations only below 200K: the loop containing residues 79-83 (**Figure 4, Movie 3**). This region is well fit by a single conformation at each temperature above the glass transition, but a secondary loop conformation is necessary to explain the electron density at 100, 150, and 180 K. Additionally, the loop is clearly single-state in the highest-resolution (1.2 Å) dataset, which is at room temperature (**Figure 4 - S1**) – demonstrating that the slightly lower resolution of the elevated temperature datasets is not responsible for obscuring the secondary conformation.

In the primary conformation, the 79-83 loop is not involved in any mainchain-mainchain hydrogen bonds to the rest of CypA, suggesting that the barrier to forming the secondary conformation does not involve breakage of cooperative secondary-structure-like interactions. Given that relative enthalpic contributions to free energy are

bioRxiv preprint doi: https://doi.org/10.1101/016733; this version posted March 19, 2015. The copyright holder for this preprint (which was not certified by peer review) is the author/funder, who has granted bioRxiv a license to display the preprint in perpetuity. It is made available under aCC-BY 4.0 International license.

increased at lower temperatures (Halle, 2004; Keedy et al., 2014), these observations indicate that the appearance of the secondary state for residues 79-83 at 100-180 K, but not at 240-310 K, is enthalpically driven, in agreement with theoretical predictions (Halle, 2004; Prell et al., 2010). Consistent with an enthalpic stabilization mechanism, the secondary conformation of the 79-83 loop is accompanied by an ordered, partial-occupancy water molecule (**Figure 4**, top row). This water molecule, which is clearly distinct from the carbonyl oxygen of the primary conformation of Glu81, wedges between the loop and the rest of the protein.

The conformational dynamics of this loop play a role in the evolution of HIV restriction by CypA fusion proteins. The antiretroviral TRIMCyp fusion protein RhTC from rhesus macaque, which has evolved to specifically prevent HIV-2 propagation, is identical to human CypA in the Cyp domain, except for the D66N and R69H mutations in the loop structurally adjacent to the 79-83 loop. Interestingly, although the 1.5 Å structure of this TRIMCyp was determined at 100 K (PDB ID 2wlw), the 79-83 loop adopts only the single conformation observed above 200 K in our structures of CypA, apparently because of electrostatic interactions and a water-bridged hydrogen bond between His69 and Glu81 (Price et al., 2009) (**Figure 4 – Figure Supplement 2**). Thus, multiple loops in CypA are flexible yet can be rigidified: the 65-75 loop by mutation in an evolutionary "arms race" with HIV or, for the 79-83 loop, by temperatures that favor entropic release of the ordered water. The surprising appearance of specific solvent-linked protein conformational heterogeneity exclusively below 200 K emphasizes the complex and heterogeneous changes in protein energetics that can occur across the glass transition.

Quantifying Changes in Conformational Heterogeneity Across the Glass Transition

Despite the counterexample of the 79-83 loop, many residues in CypA, especially in the active site, exhibit increases in discrete conformational heterogeneity above the glass transition temperature. To quantify these changes, we summed the electron density in the volume that is occupied exclusively by the minor conformations of Ser99 and Phe114, and avoided any voxels that overlap with the van der Waals radii of atoms of the major conformations (**Figure 5A**). This procedure directly reports on the non-harmonic effects that are poorly modeled by the simple B-factor approximation in single-conformer models used in previous studies of the glass transition (Frauenfelder et al., 1987; Tilton et al., 1992). The resulting curves of minor-state electron density vs. temperature are shallow at low temperature and we observe that evidence for the alternative conformations is essentially linearly amplified by increases in temperature only above ~200K (**Figure 5B,C**). The electron density for the XFEL data is consistent with the data collection temperature (273 K) and the overall trends. The inflection point is in a similar temperature range to previous reports of a protein "glass transition" around 180-220 K based on many biophysical probes, including NMR order parameters in calmodulin (Lee and Wand, 2001) and averaged isotropic B-factors in ribonuclease A (Rasmussen et al., 1992) and myoglobin (Frauenfelder et al., 1987).

bioRxiv preprint doi: https://doi.org/10.1101/016733; this version posted March 19, 2015. The copyright holder for this preprint (which was not certified by peer review) is the author/funder, who has granted bioRxiv a license to display the preprint in perpetuity. It is made available under aCC-BY 4.0 International license.

However, many residues do not have such easily characterized and separable regions of electron density. To separate out the harmonic from the non-harmonic contributions to conformational heterogeneity across the glass transition throughout CypA, we used B-factor-dependent crystallographic order parameters (S^2) (Fenwick et al., 2014). These order parameters demonstrate good agreement NMR relaxation measurements (Fenwick et al., 2014) and are calculated by weighting harmonic motions within energy basins (encoded by B-factors) and non-harmonic motions between energy basins such as separate rotamers (encoded by occupancies and displacements in coordinates). In agreement with the electron density quantification results, we observed a large change in χ1 bond order parameters above the glass transition temperature (**Figure 6A**). Decomposing the order parameter into the B-factor and occupancy components revealed a major contribution of the shift between alternative conformations (**Figure 6A - S2**). This result is in line with classic work suggesting that proteins interconvert between hierarchies of states defined by tiered energy landscapes (Frauenfelder et al., 1991).

Although conformational heterogeneity increases with temperature throughout the enzyme, there is a diversity of detailed conformational responses. For example, the distribution of intersection temperatures for the <200 K and >200 K fit lines in **Figure 6A** has a broad and asymmetrical distribution with an elongated tail from the peak near 250 K toward 200 K (**Figure 6B**), suggesting that different residues experience dynamic transitions at different temperatures. Furthermore, conformational responses are more varied (**Figure 6 - S1 A)** and the distribution of intersection temperatures is more complex for order parameters reporting on the terminal heavy atom bond of the side chain than for χ1 (**Figure 6 - S1 B**). This increase likely occurs because sidechain end orientations are subject to more degrees of freedom and therefore temperature change may redistribute them in a greater variety of ways. Overall, these results evoke a complex conformational landscape for CypA with "molten" sidechain behavior even in the protein core (Lindorff-Larsen et al., 2005).

A Hierarchy of Coupling Between Active-Site Residues

While the results above show a variety of non-linear conformational responses around the glass transition, it remains unclear whether these responses have their origin in coupled conformational shifts involving multiple residues. In particular, the network of alternative sidechain conformations spreading from the core of the protein (Ser99) into the active site (Arg55) across multiple β-strands exhibits qualitatively similar behavior of increasing occupancy above 240 K. In previous work (Fraser et al., 2009), the collective appearance of these alternative conformations at room temperature, but not at cryogenic temperatures, and the close contacts between these residues had suggested a single exchange process for this dynamic active site network. However, using our new multitemperature data, this network appears subdivided based on the apparent dynamic transition temperatures of the constituent residues, with Ser99 and Phe113 behaving most similarly to each other (**Figure 7, Movie 4**). We estimated K_{eq} for the major-to-minor transition of each of the residues displaying alternative conformations in the active-site dynamic network based on ratios of crystallographic occupancies. While true Van't Hoff analysis assumes that ΔH is constant across the temperature range, the complex changes that occur across the glass

bioRxiv preprint doi: https://doi.org/10.1101/016733; this version posted March 19, 2015. The copyright holder for this preprint (which was not certified by peer review) is the author/funder, who has granted bioRxiv a license to display the preprint in perpetuity. It is made available under aCC-BY 4.0 International license.

transition limited our analysis here to temperatures >200 K. Given these caveats, however, our "pseudo Van't Hoff" analysis suggests that Ser99 and Phe113 experience similar thermodynamic changes when transitioning from the major to the minor conformation: the minor conformations are less enthalpically stable by a few kcal/mol, but more entropically stable near physiological temperature by a similar amount (**Figure 8**, top row). By contrast, Met61 has smaller entropy and enthalpy changes, and the minor state for Arg55 is stabilized enthalpically rather than entropically (**Figure 8**, bottom row).

Discussion

Here we have mapped the conformational landscape of the dynamic enzyme CypA by a two-pronged strategy. First, we determined a high-resolution crystal structure of CypA using fixed-target SF-ROX data collection with the X-ray free electron laser. Because XFEL diffraction and data collection occur on a faster timescale than chemical damage to the crystal by incident X-rays, this structure is effectively free of radiation damage. As has been observed for the serotonin receptor GPCR, the conformations imaged by room temperature XFEL experiments can deviate from the cryogenic structrues determined at synchrotron sources (Liu et al., 2013). In contrast to that SFX experiment, which used ~30,000 diffraction images, the advances made possible by post-refinement (Uervirojnangkoorn et al., 2015) and goniometer-based crystallography (Cohen et al., 2014) at LCLS enabled data collection from only 1,239 images. Therefore our XFEL results bridge previous solution experiments with room-temperature synchrotron crystallography by demonstrating the structural origin of the active-site conformational heterogeneity of CypA free from any radiation damage artifacts.

Second, we characterized the conformational landscape of CypA by multitemperature crystallography. Previous approaches to studying the glass transition across the 180-220 K temperature regime were limited in different ways: Mössbauer spectroscopy (Parak et al., 1981) is restricted to metal sites, inelastic neutron scattering (Doster et al., 1989) gives only globally averaged information about motions, crystallographic B-factors (Frauenfelder et al., 1987; Tilton et al., 1992) and NMR order parameters (Lee and Wand, 2001) are site-resolved but cannot distinguish between different types of motions, and molecular dynamics simulations (Vitkup et al., 2000) explicitly monitor all protein and solvent atoms but are subject to imperfections in the underlying energy function and limited sampling time. By contrast, our multiconformer crystallographic models include both B-factors and explicit occupancy-weighted alternative conformations, granting us experimentally-based, site-resolved insight into the conformational response to temperature perturbation. We observed many abrupt effects of temperature titration: for example, active-site conformational heterogeneity increases dramatically above 200 K, whereas one loop adopts alternative conformations only below 200 K. Interestingly, this loop interacts with an adjacent loop in response to point mutations as part of an evolutionary arms race with HIV in primates (Price et al., 2009), emphasizing the ability of multitemperature experiments to reveal conformational heterogeneity that can be acted upon by selection. Most residues experience temperature-dependent increases in conformational heterogeneity

bioRxiv preprint doi: https://doi.org/10.1101/016733; this version posted March 19, 2015. The copyright holder for this preprint (which was not certified by peer review) is the author/funder, who has granted bioRxiv a license to display the preprint in perpetuity. It is made available under aCC-BY 4.0 International license.

only above 200 K; however, this increase does not originate from a single global transition temperature and even closely packed residues in the active site dynamic network exhibit heterogeneous responses.

These findings lend support to the idea that distinct classes of functionally important protein motions are activated as temperature increases across the glass transition (Lee and Wand, 2001). In the dynamic active-site network of CypA, we observe evidence for imperfect coupling, with Ser99 and Phe113 more tightly coupled to each other than to the rest of the network. Our observations suggest that the catalytically limiting motion in the CypA active-site network, which was identified by NMR relaxation dispersion data (Eisenmesser et al., 2005; Schlegel et al., 2009), is likely comprised of many stochastic processes that occur on similar timescales. Indeed, analysis of the contacts between alternative conformations shows that many computed pathways of steric clash-relief events involve only subsets of the active-site network (van den Bedem et al., 2013). Such "frustration", and subsequent "cracking" mechanisms, are likely at play for many systems that are thought to exhibit collective and functionally important dynamics (Bhabha et al., 2014; Ferreiro et al., 2011). These phenomena may arise because there is insufficient evolutionary pressure to "perfectly" sculpt the energy basins, energy barriers, and changes thereof along the entire trajectory of a conformational change. However, selection can act to exploit the distinct substates populated by the apo native enzyme for different parts of the catalytic cycle, such as substrate binding or product release (De Simone et al., 2015).

The observation of imperfect coupling suggests that the collective fitting used for NMR relaxation data of CypA (Eisenmesser et al., 2002; Eisenmesser et al., 2005), which indicated a single common exchange process for these residues in both the apo state and during catalysis, may obscure multiple related exchange processes. Indeed, subsequent NMR relaxation experiments of mutants designed to perturb the dynamics suggested that multiple exchange processes occur across the network (Schlegel et al., 2009). Subsets of the active site may move independently, which is consistent with the idea that an ensemble of electrostatic mechanisms are exploited for catalyzing proline *cis-trans* isomerization (Camilloni et al., 2014). More generally, the hierarchy of energetic coupling inferred here is reminiscent of the view espoused by Frauenfelder and colleagues that protein energy landscapes are complex with many nested substates (Frauenfelder et al., 1991). However, to reveal the kinetic processes underlying these substates, time-resolved experiments, likely using the XFEL pump-probe setup (Tenboer et al., 2014) or next-generation synchrotron sources, will be necessary.

These new technologies will test hypotheses about the relationship between macromolecular motion and function by offering increasing access to time-resolved experiments with all-atom detail. Such experiments can potentially reveal the structural basis of protein motions and the extent of conformational coupling during functional cycles. Temperature jumps are a potentially generalizable mechanism to expose the lower-population conformations used by ligand binding or shifted by mutation (Fraser et al., 2011; Woldeyes et al., 2014). We have demonstrated here that both XFEL and multitemperature crystallography are feasible for CypA, which are prerequisites for time-

bioRxiv preprint doi: https://doi.org/10.1101/016733; this version posted March 19, 2015. The copyright holder for this preprint (which was not certified by peer review) is the author/funder, who has granted bioRxiv a license to display the preprint in perpetuity. It is made available under aCC-BY 4.0 International license.

resolved temperature-jump XFEL experiments that could directly interrogate the degree and mechanism of coupling in the active-site network (**Figure 8 - S1**). The ability to use small crystals in XFEL experiments is a major advantage for syncing reactions and penetrating samples with "pump" laser pulses (Tenboer et al., 2014). These advantages will likely extend to irreversible reactions triggered by the short diffusion times of substrates into nanocrystals (Schmidt, 2013). As more complex reactions are probed, advances in identifying (Lang et al., 2010; Rajagopal et al., 2004) and modeling (Shukla et al., 2015; van den Bedem et al., 2009) the component conformations will be required. These future studies will reveal protein conformational dynamics in atomic detail, advancing our ability to dissect native reaction mechanisms and effectively engineer artificial catalysts, biosensors, and other useful nanomachines.

Methods

Protein expression, purification, and crystallization.
Wildtype CypA was produced and crystallized as previously reported (Fraser et al., 2009). Briefly, crystals were grown by mixing equal volumes of well solution (100 mM HEPES pH 7.5, 23% PEG 3350, 5 mM TCEP) and protein (60 mg mL^{-1} in 20 mM HEPES pH 7.5, 100 mM NaCl, 0.5 mM TCEP) in the hanging-drop format.

Crystallographic data collection.
For the XFEL experiment, we collected multiple diffraction images per crystal using a 10 micron X-ray beam with each irradiation point separated by at least 25-40 microns to avoid diffusion of radiation damage. A total of 1,239 still diffraction images were collected from 71 CypA crystals over the course of two experiments using a goniometer setup and a Rayonix MX325HE detector at LCLS-XPP (Cohen et al., 2014) (**Movie 1**). All data was collected at ambient temperature (approximately 273 K). To prevent dehydration, crystals were coated with paratone oil immediately after looping and mounted on the goniometer at the XPP end station of LCLS using the SAM sample exchange robot (Cohen et al., 2002).

For the new 1.2 Å room-temperature synchrotron dataset, paratone oil was applied to cover a 2 µL hanging drop containing a single large crystal of CypA. The crystal was harvested through the paratone and excess mother liquor was removed using a fine paper wick. Attenuated data was collected at SSRL beamline 11-1 at 273 K controlled by the cryojet on the PILATUS 6M PAD detector.

For the multitemperature synchrotron datasets at 100, 150, 180, 240, 260, 280, 300, and 310 K, we collected data at the Cornell High Energy Synchrotron Source (CHESS) at beamline A1 with a 100 micron collimator using a wavelength of 0.9767 Å. Crystals were looped by hand, stripped of excess mother liquor (100 mM HEPES pH 7.5, 23% PEG 3350, 5 mM TCEP) using NVH oil (Warkentin and Thorne, 2009), and cooled, which allowed collection of complete datasets at any temperature without ice formation while avoiding use of any penetrating cryoprotectants.

Crystallographic data processing.
The synchrotron datasets were indexed, integrated, and scaled using XDS and XSCALE, and intensities were subsequently converted to structure factor amplitudes using XDSCONV. All datasets were from single crystals. Data reduction statistics for the high-resolution, room-temperature dataset and multitemperature datasets can be found in **Table 1** and **Table 3,** respectively.

bioRxiv preprint doi: https://doi.org/10.1101/016733; this version posted March 19, 2015. The copyright holder for this preprint (which was not certified by peer review) is the author/funder, who has granted bioRxiv a license to display the preprint in perpetuity. It is made available under aCC-BY 4.0 International license.

The XFEL data were processed using *cctbx.xfel* (Hattne et al., 2014). Of the 1,239 images collected, 772 were indexed and their intensities were integrated. Post-refinement, as implemented by *prime* (**p**ost-**r**ef**i**nement and **me**rging, version date: Nov 11 20:22:51 2014)(Uervirojnangkoorn et al., 2015), was used to correct the intensity measurements and merge the data. We optimized over the uc_tolerance, n-postref_cycle, sigma_min, partiality_min, and gamma_e values to obtain the final structure factor amplitudes. Data reduction statistics for the XFEL data are provided in **Table 2**.

To promote consistency between models derived from different data sets, R_{free} flags were generated using *PHENIX* for the highest-resolution "reference" (1.2 Å 273 K) dataset first, and were subsequently copied to all other multitemperature and XFEL datasets for the automated molecular replacement and refinement pipeline.

Model building.
For each dataset, we calculated initial phases by performing molecular replacement with *phenix.auto_mr* using PDB ID 2cpl as a search model. We next refined XYZs and ADPs of the initial model with *phenix.refine* for 4 macrocycles with XYZ and ADP weight optimization turned on; identified TLS groups with *phenix.find_tls_groups*; and refined optimized XYZs, ADPs, and TLS parameters for 6 more macrocycles. These single-conformer models and associated electron density maps were used as input for two subsequent steps.

First, the single-conformer models were analyzed with Ringer (Lang et al., 2010) via *mmtbx.ringer* using default settings. A coupled sidechain-backbone "backrub" motion (Davis et al., 2006) of -10˚ for Ser99 (see **Figure 4A**) was necessary to match the Cα and Cβ positions of the minor conformation as modeled in PDB ID 3K0N; using this modified backbone indeed yielded maximal minor-conformation Ringer peaks for our multitemperature datasets. No backrub motion was necessary for Leu98 due to the different type of backbone displacement (Fraser et al., 2009). Correlation coefficients between pairs of Ringer curves were calculated using the *cor* function in R (Team, 2014).

Second, the single-conformer models were used as input to *qFit* (Keedy et al., 2014; van den Bedem et al., 2009). Subsequent to the automated model building, we manually deleted ill-fitting waters and altered alternative protein sidechain conformations based on fit to the electron density in *Coot* (Emsley et al., 2010) and refinement with *phenix.refine*. For example, at 240 K, *qFit* automatically modeled Phe113 as single-state, but significant +mFo-DFc peaks remained, so we decided on a two-state model. Met61 was particularly difficult to model accurately across temperatures due to convolved issues of $\chi 3$ non-rotamericity for Met in general (Butterfoss et al., 2005), the relatively high electron count for sulfur, and likely temperature-modulated Met-specific radiation damage. For these reasons, visual inspection of the maps and manual building is currently essential for alternative backbone conformations with moderate displacements, as observed in residues 79-83 (**Figure 5**). We are currently developing new methods to automatically detect and model such backbone excursions in multiscale multiconformer models. These efforts improved R_{free} and MolProbity scores across datasets (**Table 4**). Because of the lower resolution, the XFEL model was refined with three TLS groups and with optimization of X-ray vs. geometry and ADP weights.

Model and electron density analysis.
For minor-state electron density sums, 2mFo-DFc (Fc filled) map values were summed across a grid of points defined by superimposing each model onto PDB ID 3k0n using all Cα atoms, summing the 2mFo-DFc value at each point with 0.25 Å of a target minor-state heavy atom (Oγ for Ser99; Cδ1, Cε1, Cε2, or Cζ for Phe113), and normalizing to unity across datasets for each residue being analyzed. This procedure allowed a strictly common reference set of map evaluation points. Results were very similar when using unfilled maps (data not shown).

bioRxiv preprint doi: https://doi.org/10.1101/016733; this version posted March 19, 2015. The copyright holder for this preprint (which was not certified by peer review) is the author/funder, who has granted bioRxiv a license to display the preprint in perpetuity. It is made available under aCC-BY 4.0 International license.

We calculated B-factor-influenced order parameters (S^2) as previously reported (Fenwick et al., 2014) except that we monitored one of two different types of bond vector. For the $\chi 1$ order parameter, we used Cβ-Xβ (where X = C or O) for most amino acids, Cα-Cβ for Ala, and Cα-Hα for Gly. For the sidechain-end order parameter, we used the heavy-atom to heavy-atom bond vector for each amino acid that was closest to the sidechain terminus, with ties broken by the number in the atom name (e.g. Cγ-Cδ1 instead of Cγ-Cδ2 for Leu). All negative order parameters (caused by high B-factors) were floored to 0. $\chi 1$ order parameters were floored for 7 residues, and sidechain-end order parameters were floored for 23 residues. Per-residue "apparent dynamic transition temperatures" were then calculated as the intersection between the <200 K and >200 K fit lines in order parameter vs. temperature plots and floored to 0 K if necessary. The kernel density curve was fit with the *density* function in R (Team, 2014).

For pseudo Van't Hoff analysis, K_{eq} for each residue was estimated as Q_B/Q_A where Q_A is the occupancy of alternative conformation A and Q_B is the occupancy of alternative conformation B. ΔH and ΔS for each residue were determined from the slope and intercept, respectively, of the $\log(K_{eq})$ vs. 1/T curve, and TΔS was estimated using approximately physiological temperature (310 K).

Acknowledgements
We thank Justin Biel, Bryn Fenwick, Robert Stroud, Ian Wilson, and Peter Wright for helpful conversations.
R.A.W. is supported by a NSF Graduate Research Fellowship.
M.C.T. is supported by a BioXFEL Postdoctoral Fellowship.
N.K.S. and A.S.B. are supported by NIH GM095887 and NIH GM102520
A.T.B. and W.I.W. acknowledge a Howard Hughes Medical Institute Collaborative Innovation Award (HCIA) that also provided funds for the purchase of the microdiffractometer for the goniometer setup.
H.v.d.B. is supported by the NIH Protein Structure Initiative U54GM094586 at the Joint Center for Structural Genomics and SLAC National Accelerator Laboratory grant SLAC-LDRD-0014-13-2.
R.E.T. is supported by NSF MCB-1330685.
J.S.F. is a Searle Scholar, Pew Scholar, and Packard Fellow, and is supported by NIH OD009180, NIH GM110580, and NSF STC-1231306.
Use of the Linac Coherent Light Source (LCLS), SLAC National Accelerator Laboratory, is supported by the U.S. Department of Energy, Office of Science, Office of Basic Energy Sciences under Contract No. DE-AC02-76SF00515.
Use of the Cornell High Energy Synchrotron Source (CHESS) is supported by NSF DMR-1332208. The Macromolecular Diffraction at CHESS (MacCHESS) facility is supported by NIH GM103485.
Use of the Stanford Synchrotron Radiation Lightsource, SLAC National Accelerator Laboratory, is supported by the U.S. Department of Energy, Office of Science, Office of Basic Energy Sciences under Contract No. DE-AC02-76SF00515. The SSRL Structural Molecular Biology Program is supported by the DOE Office of Biological and Environmental Research, and NIH GM103393.

The authors declare that no competing interests exist.

References

Adams, P.D., Afonine, P.V., Bunkoczi, G., Chen, V.B., Davis, I.W., Echols, N., Headd, J.J., Hung, L.W., Kapral, G.J., Grosse-Kunstleve, R.W.*, et al.* (2010). PHENIX: a comprehensive Python-based system for macromolecular structure solution. Acta crystallographica Section D, Biological crystallography *66*, 213-221.

bioRxiv preprint doi: https://doi.org/10.1101/016733; this version posted March 19, 2015. The copyright holder for this preprint (which was not certified by peer review) is the author/funder, who has granted bioRxiv a license to display the preprint in perpetuity. It is made available under aCC-BY 4.0 International license.

Baldwin, A.J., and Kay, L.E. (2009). NMR spectroscopy brings invisible protein states into focus. Nature chemical biology *5*, 808-814.

Bhabha, G., Biel, J.T., and Fraser, J.S. (2014). Keep on Moving: Discovering and Perturbing the Conformational Dynamics of Enzymes. Accounts of chemical research.

Boutet, S., Lomb, L., Williams, G.J., Barends, T.R., Aquila, A., Doak, R.B., Weierstall, U., DePonte, D.P., Steinbrener, J., Shoeman, R.L.*, et al.* (2012). High-resolution protein structure determination by serial femtosecond crystallography. Science *337*, 362-364.

Burnley, B.T., Afonine, P.V., Adams, P.D., and Gros, P. (2012). Modelling dynamics in protein crystal structures by ensemble refinement. eLife *1*, e00311.

Butterfoss, G.L., Richardson, J.S., and Hermans, J. (2005). Protein imperfections: separating intrinsic from extrinsic variation of torsion angles. Acta crystallographica Section D, Biological crystallography *61*, 88-98.

Camilloni, C., Sahakyan, A.B., Holliday, M.J., Isern, N.G., Zhang, F., Eisenmesser, E.Z., and Vendruscolo, M. (2014). Cyclophilin A catalyzes proline isomerization by an electrostatic handle mechanism. Proceedings of the National Academy of Sciences of the United States of America *111*, 10203-10208.

Cohen, A.E., Ellis, P.J., Miller, M.D., Deacon, A.M., and Phizackerley, R.P. (2002). An automated system to mount cryo-cooled protein crystals on a synchrotron beam line, using compact sample cassettes and a small-scale robot. Journal of applied crystallography *35*, 720-726.

Cohen, A.E., Soltis, S.M., Gonzalez, A., Aguila, L., Alonso-Mori, R., Barnes, C.O., Baxter, E.L., Brehmer, W., Brewster, A.S., Brunger, A.T.*, et al.* (2014). Goniometer-based femtosecond crystallography with X-ray free electron lasers. Proceedings of the National Academy of Sciences of the United States of America *111*, 17122-17127.

Davis, I.W., Arendall, W.B., 3rd, Richardson, D.C., and Richardson, J.S. (2006). The backrub motion: how protein backbone shrugs when a sidechain dances. Structure *14*, 265-274.

De Simone, A., Aprile, F.A., Dhulesia, A., Dobson, C.M., and Vendruscolo, M. (2015). Structure of a low-population intermediate state in the release of an enzyme product. eLife *4*.

Deis, L.N., Pemble, C.W.t., Qi, Y., Hagarman, A., Richardson, D.C., Richardson, J.S., and Oas, T.G. (2014). Multiscale conformational heterogeneity in staphylococcal protein a: possible determinant of functional plasticity. Structure *22*, 1467-1477.

Doster, W., Cusack, S., and Petry, W. (1989). Dynamical transition of myoglobin revealed by inelastic neutron scattering. Nature *337*, 754-756.

Dror, R.O., Dirks, R.M., Grossman, J.P., Xu, H., and Shaw, D.E. (2012). Biomolecular simulation: a computational microscope for molecular biology. Annual review of biophysics *41*, 429-452.

Eisenmesser, E.Z., Bosco, D.A., Akke, M., and Kern, D. (2002). Enzyme dynamics during catalysis. Science *295*, 1520-1523.

Eisenmesser, E.Z., Millet, O., Labeikovsky, W., Korzhnev, D.M., Wolf-Watz, M., Bosco, D.A., Skalicky, J.J., Kay, L.E., and Kern, D. (2005). Intrinsic dynamics of an enzyme underlies catalysis. Nature *438*, 117-121.

Emsley, P., Lohkamp, B., Scott, W.G., and Cowtan, K. (2010). Features and development of Coot. Acta crystallographica Section D, Biological crystallography *66*, 486-501.

bioRxiv preprint doi: https://doi.org/10.1101/016733; this version posted March 19, 2015. The copyright holder for this preprint (which was not certified by peer review) is the author/funder, who has granted bioRxiv a license to display the preprint in perpetuity. It is made available under aCC-BY 4.0 International license.

Fenwick, R.B., van den Bedem, H., Fraser, J.S., and Wright, P.E. (2014). Integrated description of protein dynamics from room-temperature X-ray crystallography and NMR. Proceedings of the National Academy of Sciences of the United States of America *111*, E445-454.

Ferreiro, D.U., Hegler, J.A., Komives, E.A., and Wolynes, P.G. (2011). On the role of frustration in the energy landscapes of allosteric proteins. Proceedings of the National Academy of Sciences of the United States of America *108*, 3499-3503.

Fraser, J.S., Clarkson, M.W., Degnan, S.C., Erion, R., Kern, D., and Alber, T. (2009). Hidden alternative structures of proline isomerase essential for catalysis. Nature *462*, 669-673.

Fraser, J.S., van den Bedem, H., Samelson, A.J., Lang, P.T., Holton, J.M., Echols, N., and Alber, T. (2011). Accessing protein conformational ensembles using room-temperature X-ray crystallography. Proceedings of the National Academy of Sciences of the United States of America *108*, 16247-16252.

Frauenfelder, H., Hartmann, H., Karplus, M., Kuntz, I.D., Jr., Kuriyan, J., Parak, F., Petsko, G.A., Ringe, D., Tilton, R.F., Jr., Connolly, M.L.*, et al.* (1987). Thermal expansion of a protein. Biochemistry *26*, 254-261.

Frauenfelder, H., Petsko, G.A., and Tsernoglou, D. (1979). Temperature-dependent X-ray diffraction as a probe of protein structural dynamics. Nature *280*, 558-563.

Frauenfelder, H., Sligar, S.G., and Wolynes, P.G. (1991). The energy landscapes and motions of proteins. Science *254*, 1598-1603.

Fukuda, Y., and Inoue, T. (2015). High-temperature and high-resolution crystallography of thermostable copper nitrite reductase. Chemical communications.

Garman, E.F. (2010). Radiation damage in macromolecular crystallography: what is it and why should we care? Acta crystallographica Section D, Biological crystallography *66*, 339-351.

Halle, B. (2004). Biomolecular cryocrystallography: structural changes during flash-cooling. Proceedings of the National Academy of Sciences of the United States of America *101*, 4793-4798.

Hattne, J., Echols, N., Tran, R., Kern, J., Gildea, R.J., Brewster, A.S., Alonso-Mori, R., Glockner, C., Hellmich, J., Laksmono, H.*, et al.* (2014). Accurate macromolecular structures using minimal measurements from X-ray free-electron lasers. Nature methods *11*, 545-548.

Henzler-Wildman, K., and Kern, D. (2007). Dynamic personalities of proteins. Nature *450*, 964-972.

Hirata, K., Shinzawa-Itoh, K., Yano, N., Takemura, S., Kato, K., Hatanaka, M., Muramoto, K., Kawahara, T., Tsukihara, T., Yamashita, E.*, et al.* (2014). Determination of damage-free crystal structure of an X-ray-sensitive protein using an XFEL. Nature methods *11*, 734-736.

Holton, J.M. (2009). A beginner's guide to radiation damage. Journal of synchrotron radiation *16*, 133-142.

Holton, J.M., and Frankel, K.A. (2010). The minimum crystal size needed for a complete diffraction data set. Acta crystallographica Section D, Biological crystallography *66*, 393-408.

Keedy, D.A., van den Bedem, H., Sivak, D.A., Petsko, G.A., Ringe, D., Wilson, M.A., and Fraser, J.S. (2014). Crystal cryocooling distorts conformational heterogeneity in a model michaelis complex of DHFR. Structure *22*, 899-910.

bioRxiv preprint doi: https://doi.org/10.1101/016733; this version posted March 19, 2015. The copyright holder for this preprint (which was not certified by peer review) is the author/funder, who has granted bioRxiv a license to display the preprint in perpetuity. It is made available under aCC-BY 4.0 International license.

Kern, J., Tran, R., Alonso-Mori, R., Koroidov, S., Echols, N., Hattne, J., Ibrahim, M., Gul, S., Laksmono, H., Sierra, R.G.*, et al.* (2014). Taking snapshots of photosynthetic water oxidation using femtosecond X-ray diffraction and spectroscopy. Nature communications *5*, 4371.

Lang, P.T., Holton, J.M., Fraser, J.S., and Alber, T. (2014). Protein structural ensembles are revealed by redefining X-ray electron density noise. Proceedings of the National Academy of Sciences of the United States of America *111*, 237-242.

Lang, P.T., Ng, H.L., Fraser, J.S., Corn, J.E., Echols, N., Sales, M., Holton, J.M., and Alber, T. (2010). Automated electron-density sampling reveals widespread conformational polymorphism in proteins. Protein science : a publication of the Protein Society *19*, 1420-1431.

Lee, A.L., and Wand, A.J. (2001). Microscopic origins of entropy, heat capacity and the glass transition in proteins. Nature *411*, 501-504.

Lindorff-Larsen, K., Best, R.B., Depristo, M.A., Dobson, C.M., and Vendruscolo, M. (2005). Simultaneous determination of protein structure and dynamics. Nature *433*, 128-132.

Liu, W., Wacker, D., Gati, C., Han, G.W., James, D., Wang, D., Nelson, G., Weierstall, U., Katritch, V., Barty, A.*, et al.* (2013). Serial femtosecond crystallography of G protein-coupled receptors. Science *342*, 1521-1524.

Moffat, K. (1989). Time-resolved macromolecular crystallography. Annual review of biophysics and biophysical chemistry *18*, 309-332.

Motlagh, H.N., Wrabl, J.O., Li, J., and Hilser, V.J. (2014). The ensemble nature of allostery. Nature *508*, 331-339.

Neutze, R., and Moffat, K. (2012). Time-resolved structural studies at synchrotrons and X-ray free electron lasers: opportunities and challenges. Current opinion in structural biology *22*, 651-659.

Neutze, R., Wouts, R., van der Spoel, D., Weckert, E., and Hajdu, J. (2000). Potential for biomolecular imaging with femtosecond X-ray pulses. Nature *406*, 752-757.

Ollikainen, N., Smith, C.A., Fraser, J.S., and Kortemme, T. (2013). Flexible backbone sampling methods to model and design protein alternative conformations. Methods in enzymology *523*, 61-85.

Parak, F., Frolov, E.N., Mossbauer, R.L., and Goldanskii, V.I. (1981). Dynamics of metmyoglobin crystals investigated by nuclear gamma resonance absorption. Journal of molecular biology *145*, 825-833.

Prell, J.S., Correra, T.C., Chang, T.M., Biles, J.A., and Williams, E.R. (2010). Entropy drives an attached water molecule from the C- to N-terminus on protonated proline. Journal of the American Chemical Society *132*, 14733-14735.

Price, A.J., Marzetta, F., Lammers, M., Ylinen, L.M., Schaller, T., Wilson, S.J., Towers, G.J., and James, L.C. (2009). Active site remodeling switches HIV specificity of antiretroviral TRIMCyp. Nature structural & molecular biology *16*, 1036-1042.

Rajagopal, S., Schmidt, M., Anderson, S., Ihee, H., and Moffat, K. (2004). Analysis of experimental time-resolved crystallographic data by singular value decomposition. Acta crystallographica Section D, Biological crystallography *60*, 860-871.

Rasmussen, B.F., Stock, A.M., Ringe, D., and Petsko, G.A. (1992). Crystalline ribonuclease A loses function below the dynamical transition at 220 K. Nature *357*, 423-424.

bioRxiv preprint doi: https://doi.org/10.1101/016733; this version posted March 19, 2015. The copyright holder for this preprint (which was not certified by peer review) is the author/funder, who has granted bioRxiv a license to display the preprint in perpetuity. It is made available under aCC-BY 4.0 International license.

Rejto, P.A., and Freer, S.T. (1996). Protein conformational substates from X-ray crystallography. Progress in biophysics and molecular biology *66*, 167-196.

Ringe, D., and Petsko, G.A. (2003). The 'glass transition' in protein dynamics: what it is, why it occurs, and how to exploit it. Biophysical chemistry *105*, 667-680.

Schlegel, J., Armstrong, G.S., Redzic, J.S., Zhang, F., and Eisenmesser, E.Z. (2009). Characterizing and controlling the inherent dynamics of cyclophilin-A. Protein science : a publication of the Protein Society *18*, 811-824.

Schlichting, I. (2015). Structural biology: Photosynthetic complex in close-up. Nature *517*, 26-27.

Schmidt, M. (2013). Mix and Inject: Reaction Initiation by Diffusion for Time-Resolved Macromolecular Crystallography. Advances in Condensed Matter Physics *2013*, 167276.

Shukla, D., Hernandez, C.X., Weber, J.K., and Pande, V.S. (2015). Markov State Models Provide Insights into Dynamic Modulation of Protein Function. Accounts of chemical research.

Smith, J.L., Hendrickson, W.A., Honzatko, R.B., and Sheriff, S. (1986). Structural heterogeneity in protein crystals. Biochemistry *25*, 5018-5027.

Spence, J.C., Weierstall, U., and Chapman, H.N. (2012). X-ray lasers for structural and dynamic biology. Reports on progress in physics Physical Society *75*, 102601.

Suga, M., Akita, F., Hirata, K., Ueno, G., Murakami, H., Nakajima, Y., Shimizu, T., Yamashita, K., Yamamoto, M., Ago, H.*, et al.* (2015). Native structure of photosystem II at 1.95 A resolution viewed by femtosecond X-ray pulses. Nature *517*, 99-103.

Team, R. (2014). R: A Language and Environment for Statistical Computing (Vienna, Austria: R Foundation for Statistical Computing).

Tenboer, J., Basu, S., Zatsepin, N., Pande, K., Milathianaki, D., Frank, M., Hunter, M., Boutet, S., Williams, G.J., Koglin, J.E.*, et al.* (2014). Time-resolved serial crystallography captures high-resolution intermediates of photoactive yellow protein. Science *346*, 1242-1246.

Tilton, R.F., Jr., Dewan, J.C., and Petsko, G.A. (1992). Effects of temperature on protein structure and dynamics: X-ray crystallographic studies of the protein ribonuclease-A at nine different temperatures from 98 to 320 K. Biochemistry *31*, 2469-2481.

Trincao, J., Hamilton, M.L., Christensen, J., and Pearson, A.R. (2013). Dynamic structural science: recent developments in time-resolved spectroscopy and X-ray crystallography. Biochemical Society transactions *41*, 1260-1264.

Uervirojnangkoorn, M., Zeldin, O.B., Lyubimov, A.Y., Hattne, J., Brewster, A.S., Sauter, N.K., Weis, W.I., and Brunger, A.T. (2015). Enabling X-ray Free Electron Laser Crystallography for Challenging Biological Systems from a Limited Number of Crystals. eLife *In Press*.

van den Bedem, H., Bhabha, G., Yang, K., Wright, P.E., and Fraser, J.S. (2013). Automated identification of functional dynamic contact networks from X-ray crystallography. Nature methods *10*, 896-902.

van den Bedem, H., Dhanik, A., Latombe, J.C., and Deacon, A.M. (2009). Modeling discrete heterogeneity in X-ray diffraction data by fitting multi-conformers. Acta crystallographica Section D, Biological crystallography *65*, 1107-1117.

bioRxiv preprint doi: https://doi.org/10.1101/016733; this version posted March 19, 2015. The copyright holder for this preprint (which was not certified by peer review) is the author/funder, who has granted bioRxiv a license to display the preprint in perpetuity. It is made available under aCC-BY 4.0 International license.

van den Bedem, H., and Fraser, J.S. (2015). Integrative, Dynamic Structural Biology at Atomic Resolution—It's About Time. Nature methods *In Press*.

Vitkup, D., Ringe, D., Petsko, G.A., and Karplus, M. (2000). Solvent mobility and the protein 'glass' transition. Nature structural biology *7*, 34-38.

Warkentin, M., Hopkins, J.B., Badeau, R., Mulichak, A.M., Keefe, L.J., and Thorne, R.E. (2013). Global radiation damage: temperature dependence, time dependence and how to outrun it. Journal of synchrotron radiation *20*, 7-13.

Warkentin, M., Hopkins, J.B., Haber, J.B., Blaha, G., and Thorne, R.E. (2014). Temperature-dependent radiation sensitivity and order of 70S ribosome crystals. Acta crystallographica Section D, Biological crystallography *70*, 2890-2896.

Warkentin, M., and Thorne, R.E. (2009). Slow cooling of protein crystals. Journal of applied crystallography *42*, 944-952.

White, T.A., Barty, A., Stellato, F., Holton, J.M., Kirian, R.A., Zatsepin, N.A., and Chapman, H.N. (2013). Crystallographic data processing for free-electron laser sources. Acta crystallographica Section D, Biological crystallography *69*, 1231-1240.

Woldeyes, R.A., Sivak, D.A., and Fraser, J.S. (2014). E pluribus unum, no more: from one crystal, many conformations. Current opinion in structural biology *28*, 56-62.

Zeldin, O.B., Brockhauser, S., Bremridge, J., Holton, J.M., and Garman, E.F. (2013). Predicting the X-ray lifetime of protein crystals. Proceedings of the National Academy of Sciences of the United States of America *110*, 20551-20556.

bioRxiv preprint doi: https://doi.org/10.1101/016733; this version posted March 19, 2015. The copyright holder for this preprint (which was not certified by peer review) is the author/funder, who has granted bioRxiv a license to display the preprint in perpetuity. It is made available under aCC-BY 4.0 International license.

Movie 1: Fixed-target XFEL data collection from CypA crystals at LCLS XPP end station. Screen capture image of the Blu-Ice GUI showing a video display of a CypA crystal. After each shot, a new damage line appears and the crystal is translated.

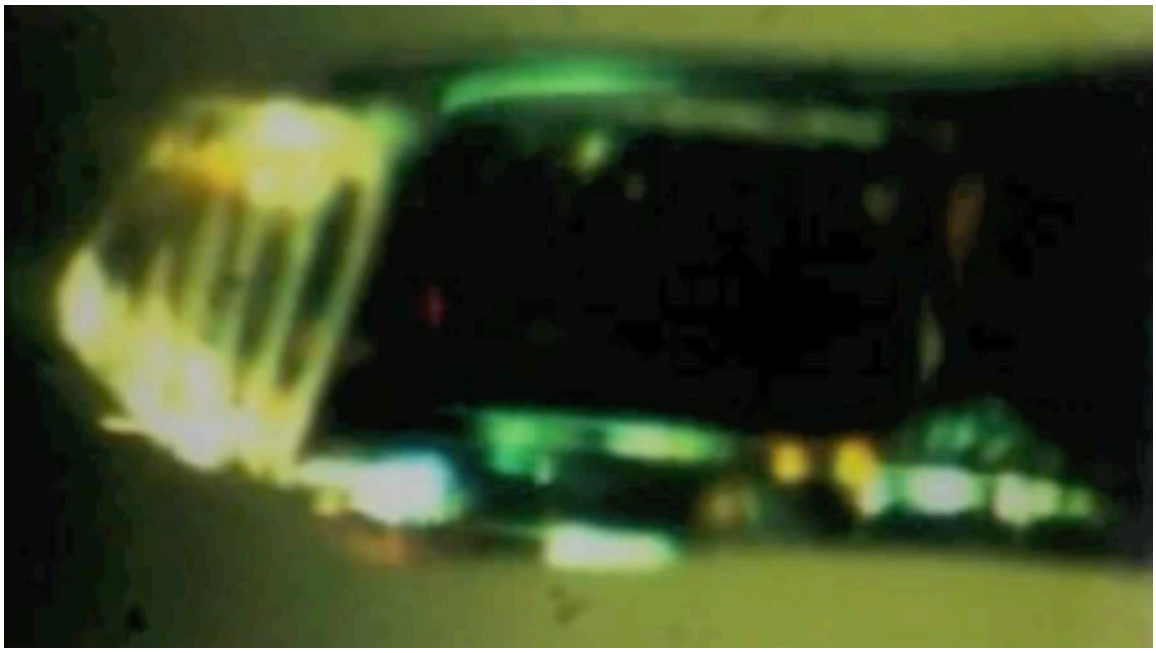

bioRxiv preprint doi: https://doi.org/10.1101/016733; this version posted March 19, 2015. The copyright holder for this preprint (which was not certified by peer review) is the author/funder, who has granted bioRxiv a license to display the preprint in perpetuity. It is made available under aCC-BY 4.0 International license.

	1.2 Å synchrotron
PDB ID	4YUO
Wavelength	0.9795
Resolution range	44.60 - 1.20 (1.24 - 1.20)
Space group	P 21 21 21
Unit cell	42.9 52.43 89.11 90 90 90
Total reflections	307722 (18999)
Unique reflections	58118 (5122)
Multiplicity	5.3 (3.7)
Completeness (%)	91 (82)
Mean I/sigma(I)	10.99 (5.93)
Wilson B-factor	15.22
R-merge (%)	11.2 (20.4)
R-meas (%)	12.2 (23.4)
CC1/2	0.99 (0.96)
CC*	1.00 (0.99)
Refinement resolution range	45.19 - 1.20 (1.23 - 1.20)
Reflections used in refinement	58108 (3657)
Reflections used for R-free	2000 (126)
R-work (%)	12.7 (31.3)
R-free (%)	14.6 (33.5)
Number of non-hydrogen atoms	2327
Macromolecular atoms	2143
Protein residues	163
RMS(bonds)	0.009
RMS(angles)	1.16
Ramachandran favored (%)	96
Ramachandran allowed (%)	4.1
Ramachandran outliers (%)	0
Rotamer outliers (%)	0.84
Clashscore	0.98
Average B-factor	19.62
macromolecules	18.40
solvent	33.86

Table 1: Crystallographic statistics for room-temperature synchrotron dataset collected on a single crystal. Statistics for the highest-resolution shell are shown in parentheses.

bioRxiv preprint doi: https://doi.org/10.1101/016733; this version posted March 19, 2015. The copyright holder for this preprint (which was not certified by peer review) is the author/funder, who has granted bioRxiv a license to display the preprint in perpetuity. It is made available under aCC-BY 4.0 International license.

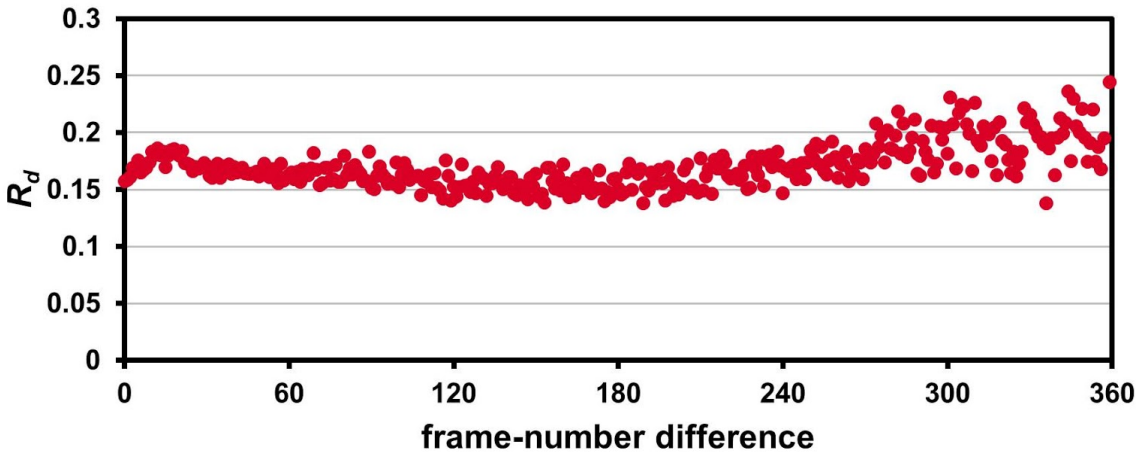

Table 1 - Figure Supplement 1: The 1.2 Å room-temperature CypA synchrotron data shows no signs of radiation damage. A plot of "decay *R*-factor" (R_d) as a function of frame-number difference has a slope of zero, indicating the absence of radiation damage. R_d is calculated using pairwise observations of unique reflections (*hkl*) with centroids on frames *i* and *j*, and the frame-number difference is given by |*i*-*j*|. The calculations were performed using a 2.0Å resolution cutoff.

bioRxiv preprint doi: https://doi.org/10.1101/016733; this version posted March 19, 2015. The copyright holder for this preprint (which was not certified by peer review) is the author/funder, who has granted bioRxiv a license to display the preprint in perpetuity. It is made available under aCC-BY 4.0 International license.

	XFEL
PDB ID	4YUP
Resolution range	43.98 - 1.75 (1.81 - 1.75)
Space group	$P2_12_12_1$
Unit cell (a, b, c)	42.42 51.82 87.96
Unique reflections	19942 (1894)
Completeness (%)	99 (96)
Wilson B-factor	21.12
Refinement resolution range	43.98 - 1.75 (1.93 - 1.75)
Reflections used in refinement	19936 (4811)
Reflections used for R-free	625 (151)
R-work (%)	20.0 (34.3)
R-free (%)	24.9 (36.1)
Number of non-hydrogen atoms	1762
Macromolecular atomcs	1559
Protein residues	164
RMS(bonds)	0.017
RMS(angles)	1.44
Ramachandran favored (%)	96
Ramachandran allowed (%)	3.6
Ramachandran outliers (%)	0
Rotamer outliers (%)	1.8
Clashscore	1.92
Average B-factor	29.03
macromolecules	26.52
solvent	48.25
Number of TLS groups	3

Table 2: Crystallographic statistics for room-temperature XFEL dataset collected across 71 crystals. Statistics for the highest-resolution shell are shown in parentheses.

bioRxiv preprint doi: https://doi.org/10.1101/016733; this version posted March 19, 2015. The copyright holder for this preprint (which was not certified by peer review) is the author/funder, who has granted bioRxiv a license to display the preprint in perpetuity. It is made available under aCC-BY 4.0 International license.

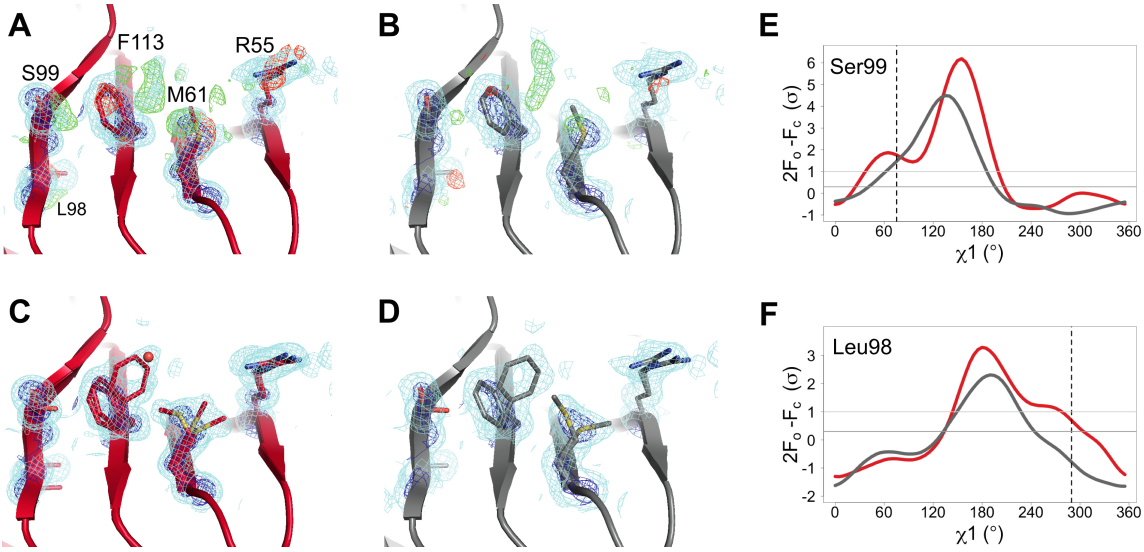

Figure 1: The active-site conformational ensemble of CypA imaged without radiation damage at room temperature. (A) Electron density maps for room-temperature synchrotron (red) and (**B**) XFEL (silver) single-conformer models reveal conformational heterogeneity extending from the protein core (Leu98 and Ser99) to the active site (Arg55) of CypA. The primary conformation is well supported by 2mFo-DFc electron density contoured at 0.6 σ (cyan mesh) and 3.0 σ (dark blue mesh). mFo-DFc difference electron density contoured at 3.0 σ (green mesh) and -3.0 σ (red mesh) suggest unmodeled alternative conformations. **(C,D)** Finalized multiconformer models explicitly model these alternative conformations, which are well-supported by 2mFo-DFc electron density. **(E,F)** Ringer electron-density sampling for the single-conformer models shows peaks representing alternative conformations for **(E)** Ser99 and **(F)** Leu98. The primary conformations of both residues are obvious as peaks for both models, but the minor conformations (dashed vertical line; as modeled in 3k0n) are also clearly evident, with 2mFo-DFc values well above the 0.3 σ (darker gray horizontal line) threshold. A backrub motion of -10˚ positions the backbone properly for Ringer to best detect the minor conformation for Ser99, but not for Leu98.

bioRxiv preprint doi: https://doi.org/10.1101/016733; this version posted March 19, 2015. The copyright holder for this preprint (which was not certified by peer review) is the author/funder, who has granted bioRxiv a license to display the preprint in perpetuity. It is made available under aCC-BY 4.0 International license.

	100 K	**150 K**	**180 K**	**240 K**	**260 K**	**280 K**	**300 K**	**310 K**
PDB ID	4YUG	4YUH	4YUI	4YUJ	4YUK	4YUL	4YUM	4YUN
Wavelength	0.9767	0.9767	0.9767	0.9767	0.9767	0.9767	0.9767	0.9767
Resolution range	33.58 - 1.48 (1.53 - 1.48)	16.95 - 1.34 (1.39 - 1.34)	16.12 - 1.38 (1.43 - 1.38)	34.05 - 1.42 (1.47 - 1.42)	33.98 - 1.48 (1.53 - 1.48)	25.23 - 1.42 (1.47 - 1.42)	22.67 - 1.5 (1.55 - 1.50)	22.66 - 1.58 (1.64 - 1.58)
Space group	$P2_12_12_1$	$P2_12_12_1$	$P2_12_12_1$	$P2_12_12_1$	$P2_12_12_1$	$P2_12_12_1$	$P2_12_12_1$	$P2_12_12_1$
Unit cell (a, b, c)	42.24 51.91 88.06	42.45 51.82 88.01	42.42 51.96 88.21	43.04 53.22 88.63	43.09 52.79 88.81	43.00 52.61 89.12	43.01 52.61 89.32	42.85 52.58 89.41
Total reflections	160129 (15842)	160780 (7437)	154202 (11295)	152578 (13600)	134699 (13381)	168932 (15019)	144734 (14433)	125225 (12326)
Unique reflections	32657 (3240)	42288 (3471)	39548 (3820)	38881 (3710)	34411 (3391)	38763 (3794)	32999 (3254)	28291 (2760)
Multiplicity	4.9 (4.9)	3.8 (2.1)	3.9 (3.0)	3.9 (3.7)	3.9 (3.9)	4.4 (4.0)	4.4 (4.4)	4.4 (4.5)
Completeness (%)	99 (100)	95 (80)	97 (95)	99 (96)	100 (100)	100 (100)	99 (100)	100 (100)
Mean I/sigma(I)	14.07 (1.57)	25.95 (3.24)	16.47 (1.64)	12.86 (1.66)	10.09 (1.46)	15.51 (1.52)	16.90 (1.63)	13.26 (1.45)
Wilson B-factor	16.07	13.12	16.95	15.55	16.06	17.62	19.75	21.44
R-merge (%)	6.8 (99.4)	3.0 (29.4)	4.2 (71.8)	6.2 (99.2)	8.1 (104.3)	4.9 (100.0)	4.7 (101.7)	6.7 (127.3)
R-meas (%)	7.6 (111.0)	3.4 (36.9)	4.8 (85.6)	7.2 (116.8)	9.4 (120.8)	5.6 (115.3)	5.4 (115.9)	7.6 (144.5)
CC1/2	1.00 (0.62)	1.00 (0.90)	1.00 (0.60)	1.00 (0.50)	1.00 (0.52)	1.00 (0.52)	1.00 (0.59)	1.00 (0.56)
CC*	1.00	1.00	1.00	1.00	1.00	1.00	1.00	1.00

bioRxiv preprint doi: https://doi.org/10.1101/016733; this version posted March 19, 2015. The copyright holder for this preprint (which was not certified by peer review) is the author/funder, who has granted bioRxiv a license to display the preprint in perpetuity. It is made available under aCC-BY 4.0 International license.

	(0.88)	(0.97)	(0.87)	(0.82)	(0.83)	(0.83)	(0.86)	(0.85)
Refinement resolution range	33.085 - 1.48 (1.558 - 1.48)	19.117 - 1.34 (1.394 - 1.34)	16.995 - 1.38 (1.435 - 1.38)	34.055 - 1.42 (1.477 - 1.42)	33.98 - 1.48 (1.547 - 1.48)	25.23 - 1.42 (1.477 - 1.42)	22.67 - 1.5 (1.579 - 1.5)	25.222 - 1.58 (1.679 - 1.58)
Reflections used in refinement	32627 (4654)	42278 (3932)	39545 (4265)	38879 (4161)	34411 (4237)	38762 (4256)	32999 (4643)	28287 (4632)
Reflections used for R-free	1028 (147)	1325 (125)	1238 (133)	1218 (130)	1080 (133)	1217 (133)	1036 (145)	889 (146)
R-work (%)	13.3 (20.4)	12.4 (16.4)	13.3 (25.4)	12.6 (26.3)	13.1 (26.0)	11.1 (22.6)	10.8 (20.0)	11.7 (21.8)
R-free (%)	18.3 (26.8)	15.6 (21.3)	17.5 (33.0)	15.6 (30.4)	16.8 (31.2)	14.3 (25.5)	14.4 (24.8)	15.0 (28.8)
Number of non-hydrogen atoms	2279	2433	1969	1993	2035	2120	2096	2172
Macromolecule atoms	1933	2132	1745	1750	1837	1924	1952	2061
Protein residues	165	164	164	163	163	163	163	163
RMS(bonds)	0.009	0.008	0.008	0.009	0.009	0.008	0.009	0.009
RMS(angles)	1.16	1.20	1.23	1.20	1.16	1.16	1.14	1.14
Ramachandran favored (%)	97	94	97	96	97	96	97	96
Ramachandran	3.3	5.7	2.7	4.1	3	4.2	3.3	3.9

bioRxiv preprint doi: https://doi.org/10.1101/016733; this version posted March 19, 2015. The copyright holder for this preprint (which was not certified by peer review) is the author/funder, who has granted bioRxiv a license to display the preprint in perpetuity. It is made available under aCC-BY 4.0 International license.

allowed (%)								
Ramachandran outliers (%)	0	0	0	0	0	0	0	0
Rotamer outliers (%)	2.4	1.3	0.53	1.1	1.5	1.9	1.4	0.88
Clashscore	0.57	1.08	0.00	1.24	0.27	0.78	0.52	0.00
Average B-factor	21.74	17.25	21.85	20.14	20.00	21.48	24.09	25.77
Macromolecule Average B-factor	18.48	14.67	19.99	17.95	18.17	19.61	22.82	24.94
Solvent Average B-factor	39.99	35.54	36.34	35.89	37.01	39.89	41.23	41.30

Table 3: Crystallographic statistics for multitemperature synchrotron datasets collected on a single crystal per dataset. Statistics for the highest-resolution shell are shown in parentheses.

bioRxiv preprint doi: https://doi.org/10.1101/016733; this version posted March 19, 2015. The copyright holder for this preprint (which was not certified by peer review) is the author/funder, who has granted bioRxiv a license to display the preprint in perpetuity. It is made available under aCC-BY 4.0 International license.

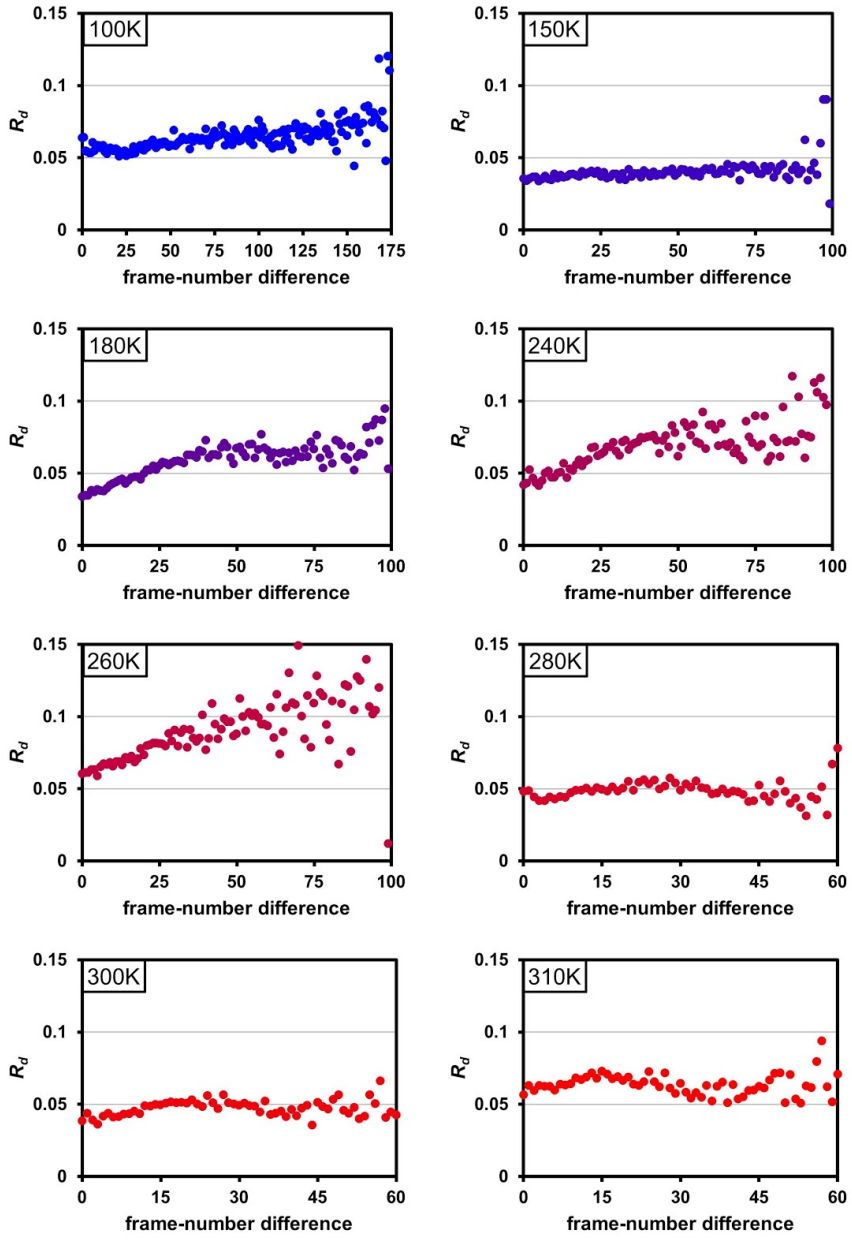

Table 3 - Figure Supplement 1: Radiation damage is minimal across data collection temperatures. Plots of R_d vs. frame-number difference (as in **Table 1 - Figure Supplement 1**) for each dataset in the multitemperature trajectory reveal only minimal radiation damage. The datasets around the glass transition temperature (180-260 K) exhibit higher R_d in later frames, which may reflect either a time-dependent cryocooling artifact or radiation damage at these intermediate temperatures. Although the rate of X-ray damage varies strongly with temperature, the data collection strategy was adjusted to yield a comparable amount of damage per frame. Therefore, there is no correlation between data collection temperature and the overall extent of radiation damage; the highest temperature data sets are equally undamaged as the lowest temperature data sets. By contrast, we observe a strong correlation between data collection temperature and conformational heterogeneity.

bioRxiv preprint doi: https://doi.org/10.1101/016733; this version posted March 19, 2015. The copyright holder for this preprint (which was not certified by peer review) is the author/funder, who has granted bioRxiv a license to display the preprint in perpetuity. It is made available under aCC-BY 4.0 International license.

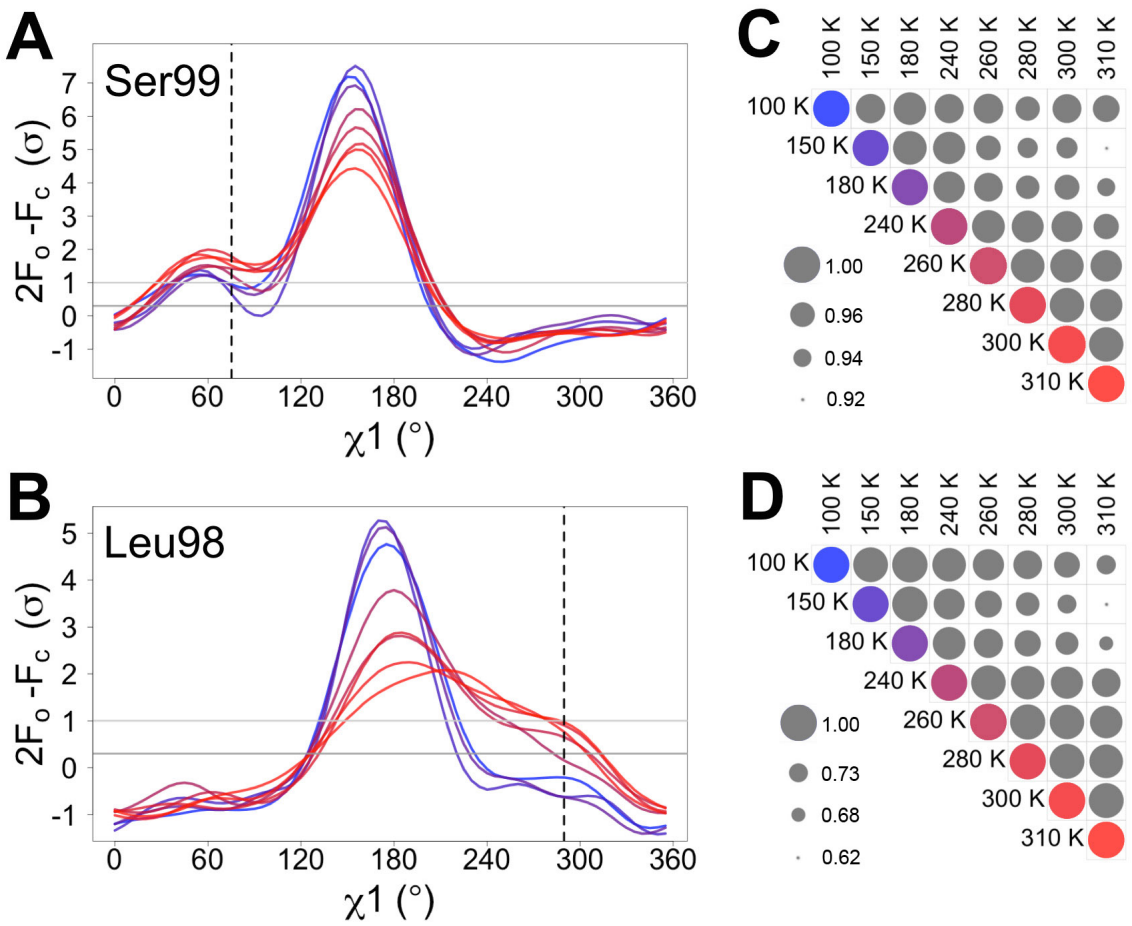

Figure 2: Automated electron density sampling reveals increased conformational redistribution above the glass transition. Ringer curves of 2mFo-DFc electron density vs. χ1 dihedral angle for **(A)** Ser99 and **(B)** Leu98 show large peaks for modeled major conformations, and also smaller peaks for additional minor conformations (dashed vertical lines). These secondary peaks become more evident as temperature increases (color gradient from blue to purple to red). A backrub motion was used for Ser99. For **(C)** Ser99 and **(D)** Leu98, a Pearson correlation coefficient was calculated between each pair of Ringer curves from the corresponding panel in **(A)** and **(B)**. Circles in diagonal elements are colored as in (**A)** and **(B)**; circles in off-diagonal elements are all gray but scaled by pairwise correlation coefficient (see legend). Pairs of curves from similar temperatures are generally more correlated to each other (larger circles) than are pairs of curves from more different temperatures (smaller circles).

bioRxiv preprint doi: https://doi.org/10.1101/016733; this version posted March 19, 2015. The copyright holder for this preprint (which was not certified by peer review) is the author/funder, who has granted bioRxiv a license to display the preprint in perpetuity. It is made available under aCC-BY 4.0 International license.

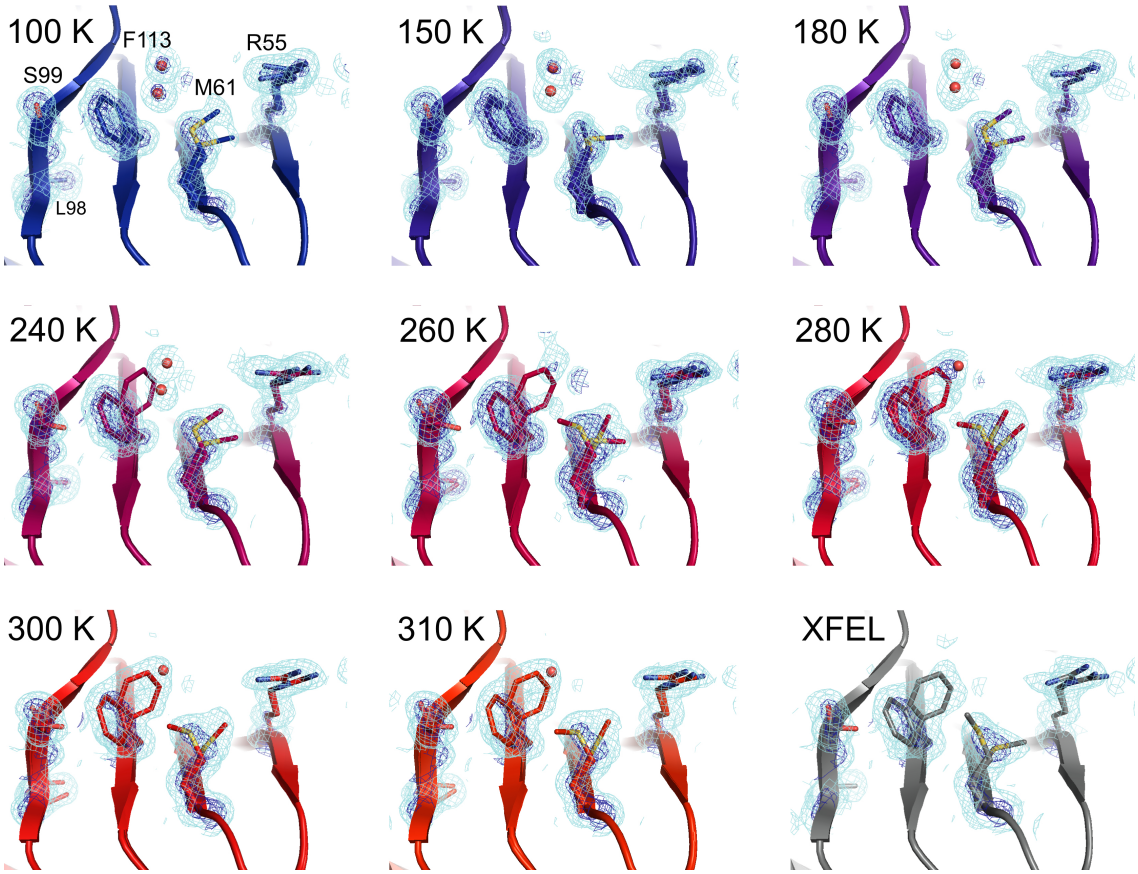

Figure 3: Multiconformer modeling across temperatures captures increasing conformational heterogeneity above the glass transition. Residues extending from the core to the active site of CypA adopt a single conformer at low temperatures, but gradually transition to increasing occupancy of secondary conformations as temperature increases above the glass transition. These conformations are well supported by 2mFo-DFc electron density contoured at 0.6 σ (cyan mesh) and 3.0 σ (dark blue mesh). This is corroborated by the room-temperature XFEL model (gray), which is free from conventional radiation damage and features the same secondary conformations. Water molecules (red spheres) are more fully ordered at low temperatures, but become only partially occupied at higher temperatures because they are mutually exclusive with the secondary Phe113 conformation.

bioRxiv preprint doi: https://doi.org/10.1101/016733; this version posted March 19, 2015. The copyright holder for this preprint (which was not certified by peer review) is the author/funder, who has granted bioRxiv a license to display the preprint in perpetuity. It is made available under aCC-BY 4.0 International license.

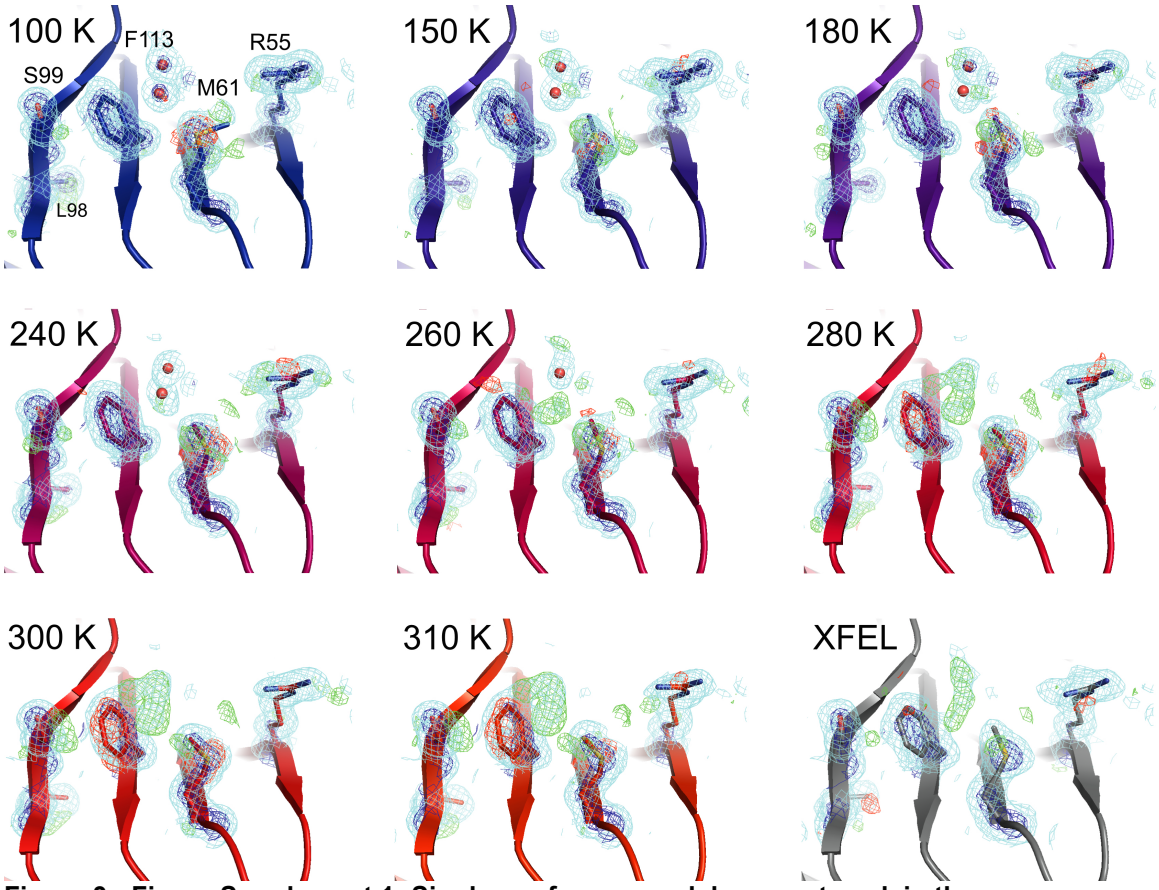

Figure 3 - Figure Supplement 1: Single-conformer models cannot explain the crystallographic data at higher temperatures. The CypA dynamic network is shown after molecular replacement and refinement (including automated water placement) in PHENIX, before any manual rebuilding. The major state is well supported by 2mFo-DFc electron density contoured at 0.6 σ (cyan mesh) and 3.0 σ (dark blue mesh) for all datasets, but mFo-DFc difference electron density becomes more negative for the major state (-3.0 σ, red mesh) and more positive for the unmodeled minor state (+3.0 σ, green mesh) as temperature increases across the synchrotron datasets (blue to red); this is especially true above the glass transition (~200 K). Full-occupancy water molecules (red spheres) are automatically placed by PHENIX near the Phe113 minor state in lower-temperature, but not in higher-temperature synchrotron models because they are mutually exclusive with the secondary Phe113 conformation.

bioRxiv preprint doi: https://doi.org/10.1101/016733; this version posted March 19, 2015. The copyright holder for this preprint (which was not certified by peer review) is the author/funder, who has granted bioRxiv a license to display the preprint in perpetuity. It is made available under aCC-BY 4.0 International license.

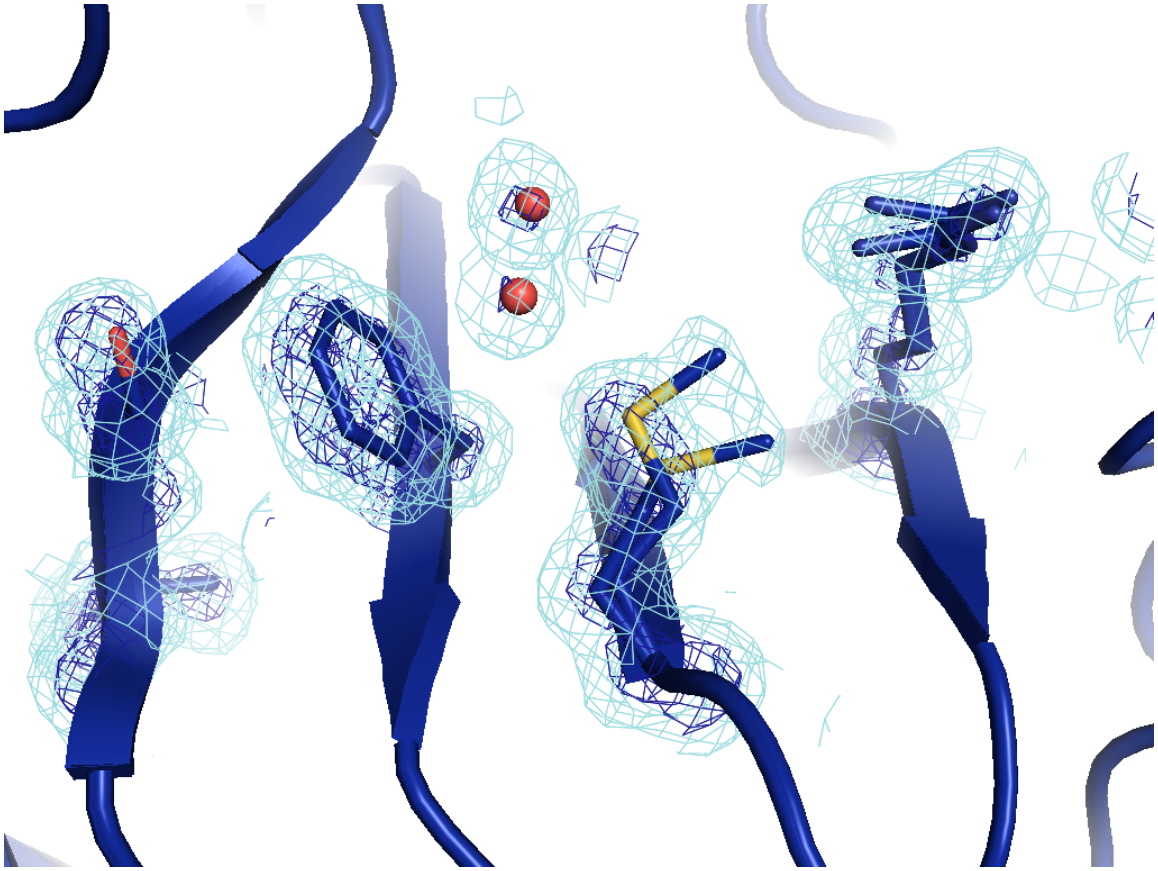

Movie 2: Animated interpolation between electron density maps in temperature trajectory. For each pair of adjacent temperatures (e.g. 100 and 150 K), the temperature regime between them was bisected and an average 2mFo-DFc electron density maps was calculated in reciprocal space using CCP4 utilities, until temperature points were spaced by <1 K. A new multiconformer model is shown when the animation reaches the corresponding temperature.

bioRxiv preprint doi: https://doi.org/10.1101/016733; this version posted March 19, 2015. The copyright holder for this preprint (which was not certified by peer review) is the author/funder, who has granted bioRxiv a license to display the preprint in perpetuity. It is made available under aCC-BY 4.0 International license.

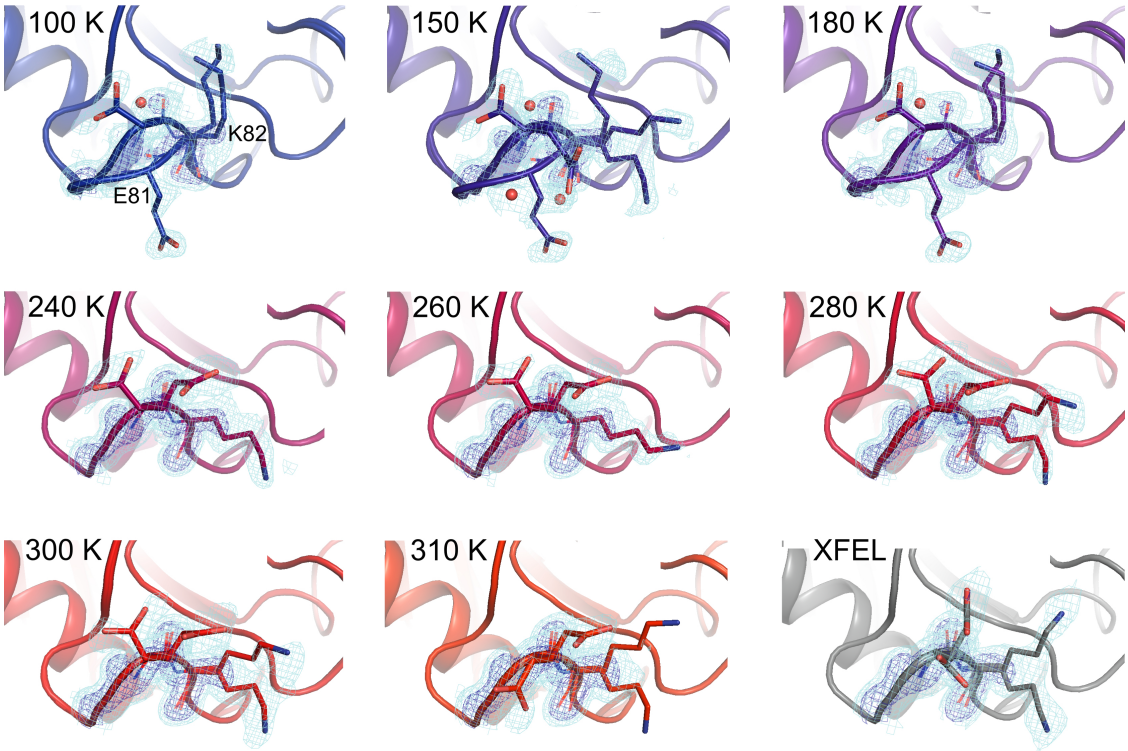

Figure 4: Low temperature "freezes in" an alternative loop conformation. The surface loop containing residues 79-83 adopts alternative conformations at temperatures below (top row) but not above (bottom two rows) the glass transition. The secondary loop conformation is separated from the body of the protein by an ordered water molecule (red sphere); the van der Waals interactions between the loop and the water may reflect an enthalpic stabilization that is more dominant at low temperatures. The electron density peak to the right of the water corresponds to the backbone carbonyl oxygen of Glu81. 2mFo-DFc electron density contoured at 0.6 σ (cyan mesh) and 2.0 σ (dark blue mesh).

bioRxiv preprint doi: https://doi.org/10.1101/016733; this version posted March 19, 2015. The copyright holder for this preprint (which was not certified by peer review) is the author/funder, who has granted bioRxiv a license to display the preprint in perpetuity. It is made available under aCC-BY 4.0 International license.

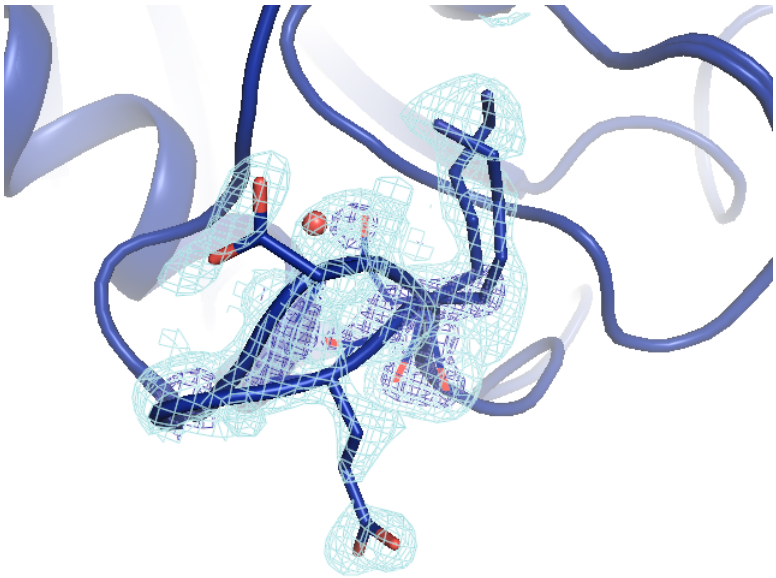

Movie 3: Animated rotation around the 100 K (blue) and 310 K (red) models and electron density maps from **Figure 4**.

bioRxiv preprint doi: https://doi.org/10.1101/016733; this version posted March 19, 2015. The copyright holder for this preprint (which was not certified by peer review) is the author/funder, who has granted bioRxiv a license to display the preprint in perpetuity. It is made available under aCC-BY 4.0 International license.

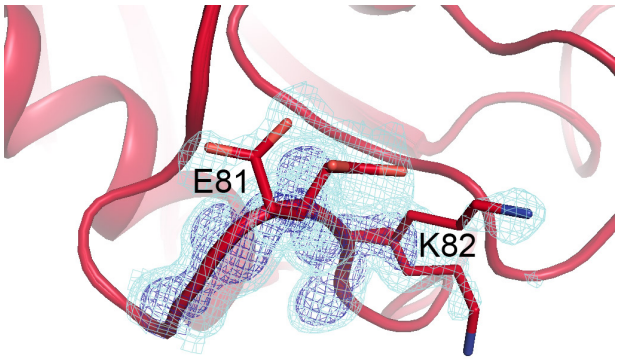

Figure 4 - Figure Supplement 1: Temperature determines a loop conformational ensemble even in the highest resolution room temperature dataset. The surface loop containing residues 79-83 adopts a single conformation at room temperature in our highest-resolution (1.2 Å) synchrotron structure.

bioRxiv preprint doi: https://doi.org/10.1101/016733; this version posted March 19, 2015. The copyright holder for this preprint (which was not certified by peer review) is the author/funder, who has granted bioRxiv a license to display the preprint in perpetuity. It is made available under aCC-BY 4.0 International license.

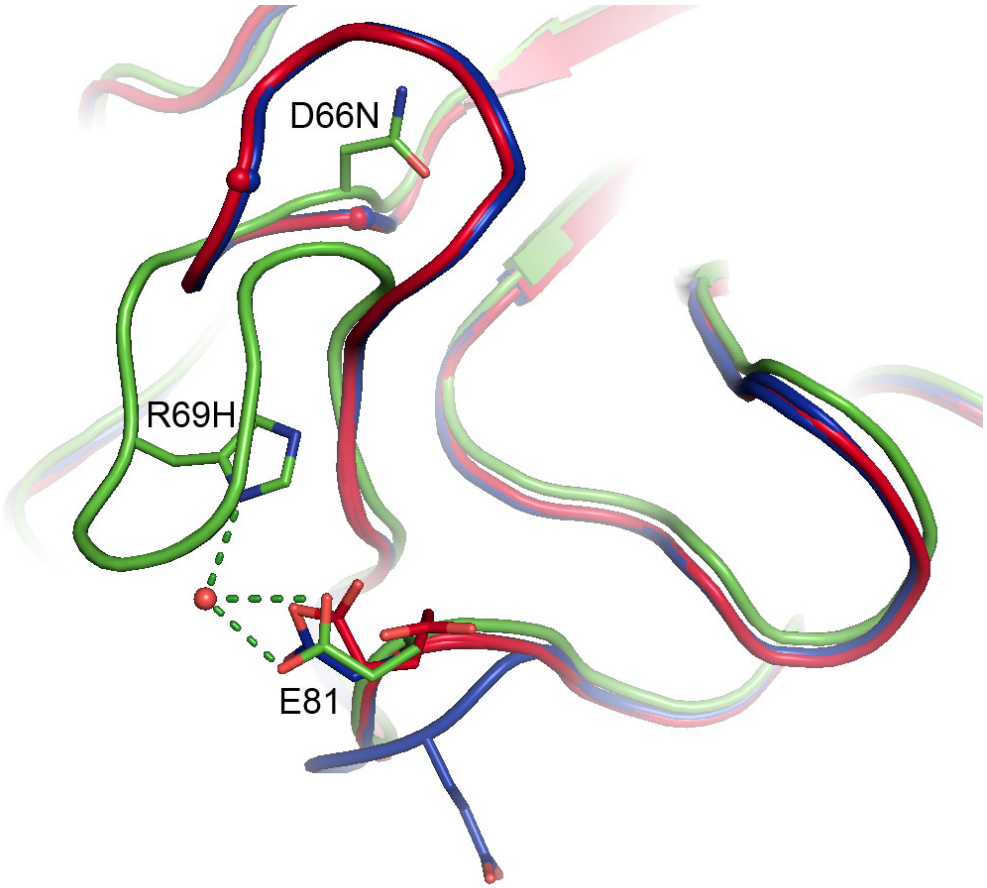

Figure 4 - Figure Supplement 2: The coupled conformational heterogeneity of two adjacent loops is revealed by temperature and evolutionary studies. Two mutations in the rhesus macaque fusion protein TRIMCyp (RhTC) relative to CypA, D66N and R69H (spheres at Cα atom in CypA), cause the loop containing residues 65-75 (top) in RhTC (green; PDB code 2wlw) to dramatically change its conformation. In the new conformation, the R69H sidechain interacts with the loop containing residues 79-83 (bottom) via hydrogen bonds (green dotted lines) with a bridging water molecule (red sphere). These interactions shift the conformational ensemble of the 79-83 loop at 100 K from two-state for CypA (blue) to single-state for RhTC (green). This interpretation for RhTC is well-supported by the electron density. This loop occupies only a single conformation in the room-temperature 1.2 Å crystal structure (red). Both loops undergo conformational exchange detectable by relaxation dispersion NMR experiments.

bioRxiv preprint doi: https://doi.org/10.1101/016733; this version posted March 19, 2015. The copyright holder for this preprint (which was not certified by peer review) is the author/funder, who has granted bioRxiv a license to display the preprint in perpetuity. It is made available under aCC-BY 4.0 International license.

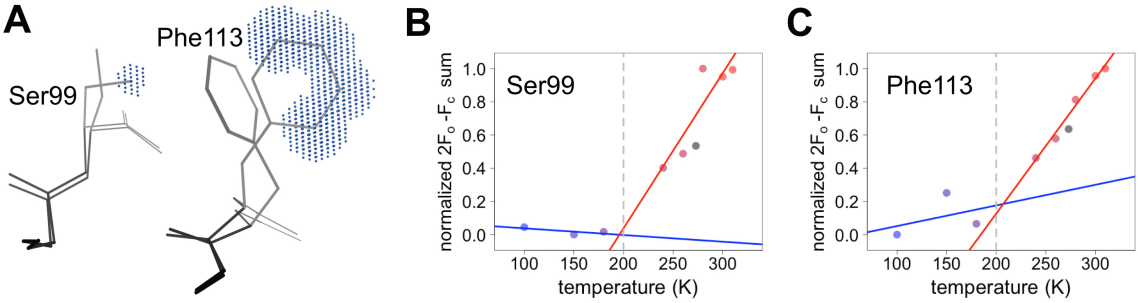

Figure 5: Quantifying temperature titration of conformational heterogeneity in multiconformer models. (A) 2mFo-DFc electron density was summed over the volume occupied by the minor conformation but not the major conformation (blue grid points) for Ser99 and Phe113. **(B,C)** Minor-state 2mFo-DFc electron density increases with temperature more rapidly above the glass transition. Electron density sums were normalized for each residue. Multitemperature points from synchrotron data is shown in colors corresponding to temperature. The XFEL point is shown in gray. Best fit lines are shown for linear trends above (red) and below (blue) 200K.

bioRxiv preprint doi: https://doi.org/10.1101/016733; this version posted March 19, 2015. The copyright holder for this preprint (which was not certified by peer review) is the author/funder, who has granted bioRxiv a license to display the preprint in perpetuity. It is made available under aCC-BY 4.0 International license.

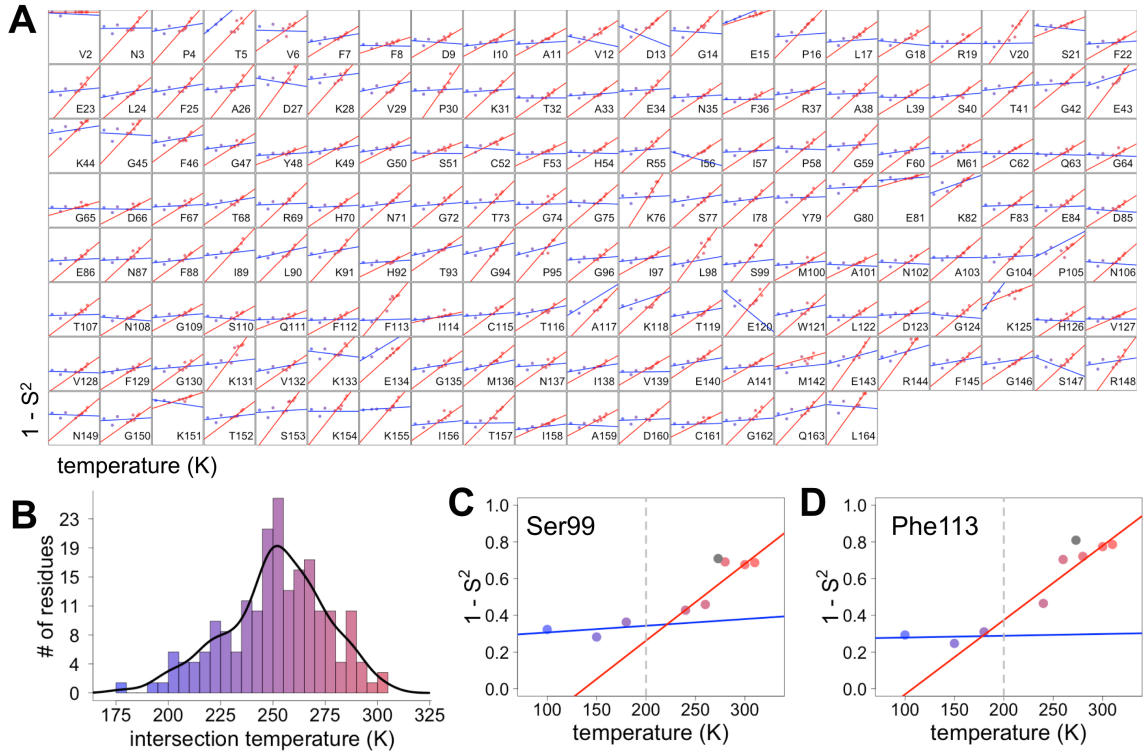

Figure 6: Sidechain order decreases with temperature more dramatically above the glass transition. (A) The complement of B-factor-influenced sidechain order parameter for the bond most closely associated with the χ1 dihedral angle for all residues in CypA. Lines reflect least-squares fits to synchrotron models below (blue) vs. above (red) the glass transition at ~200 K. **(B)** Distribution of the intersection temperature between the <200 and >200 K lines fitted with kernel density function. The peak is near 250 K, although there is a tail toward lower temperatures. Intersection temperatures were <170 K for 4 residues and >330 K for 5 residues. **(C,D)** The plots for Ser99 and Phe113 from **(A)** in more detail. Multitemperature synchrotron points in colors; XFEL points (not included in fits) in gray.

bioRxiv preprint doi: https://doi.org/10.1101/016733; this version posted March 19, 2015. The copyright holder for this preprint (which was not certified by peer review) is the author/funder, who has granted bioRxiv a license to display the preprint in perpetuity. It is made available under aCC-BY 4.0 International license.

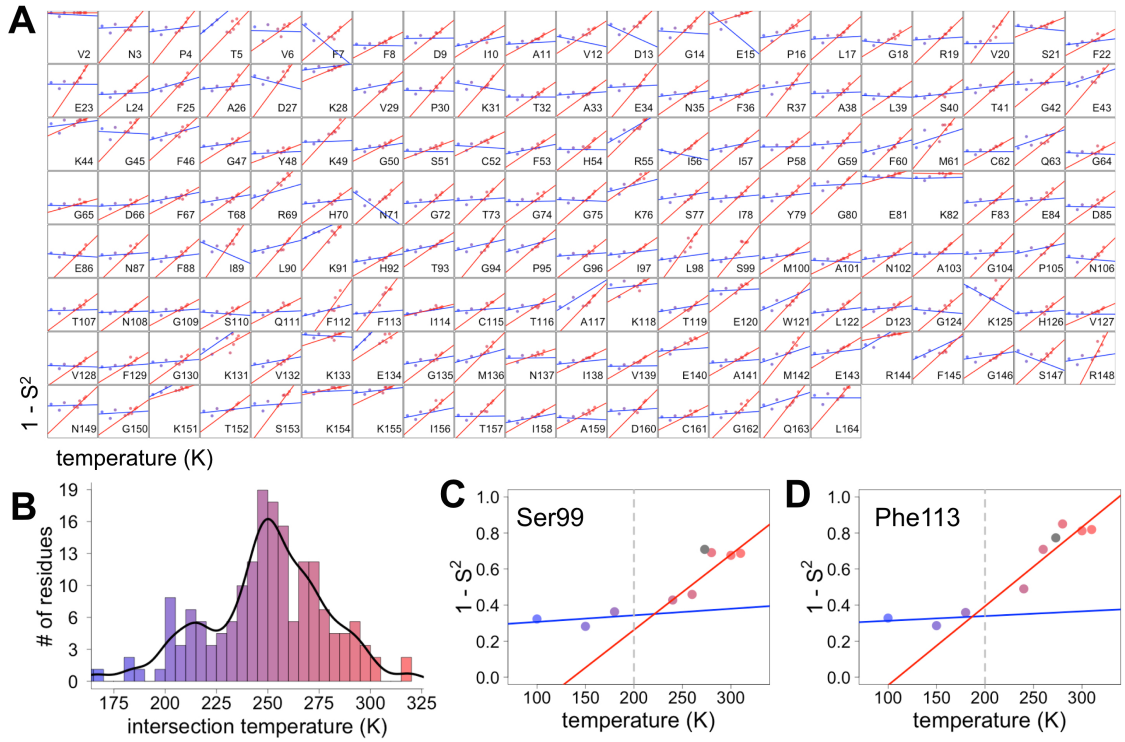

Figure 6 - Figure Supplement 1: Sidechain order for the sidechain terminus, reflecting the final heavy atom dihedral angle, also decreases with temperature more dramatically above the glass transition. Each panel is as in Figure 5, but the order parameter now models the final heavy-atom-to-heavy-atom-bond for each sidechain (see Methods). Intersection temperatures in **(B)** were <170 K for 7 residues and >330 K for 6 residues.

bioRxiv preprint doi: https://doi.org/10.1101/016733; this version posted March 19, 2015. The copyright holder for this preprint (which was not certified by peer review) is the author/funder, who has granted bioRxiv a license to display the preprint in perpetuity. It is made available under aCC-BY 4.0 International license.

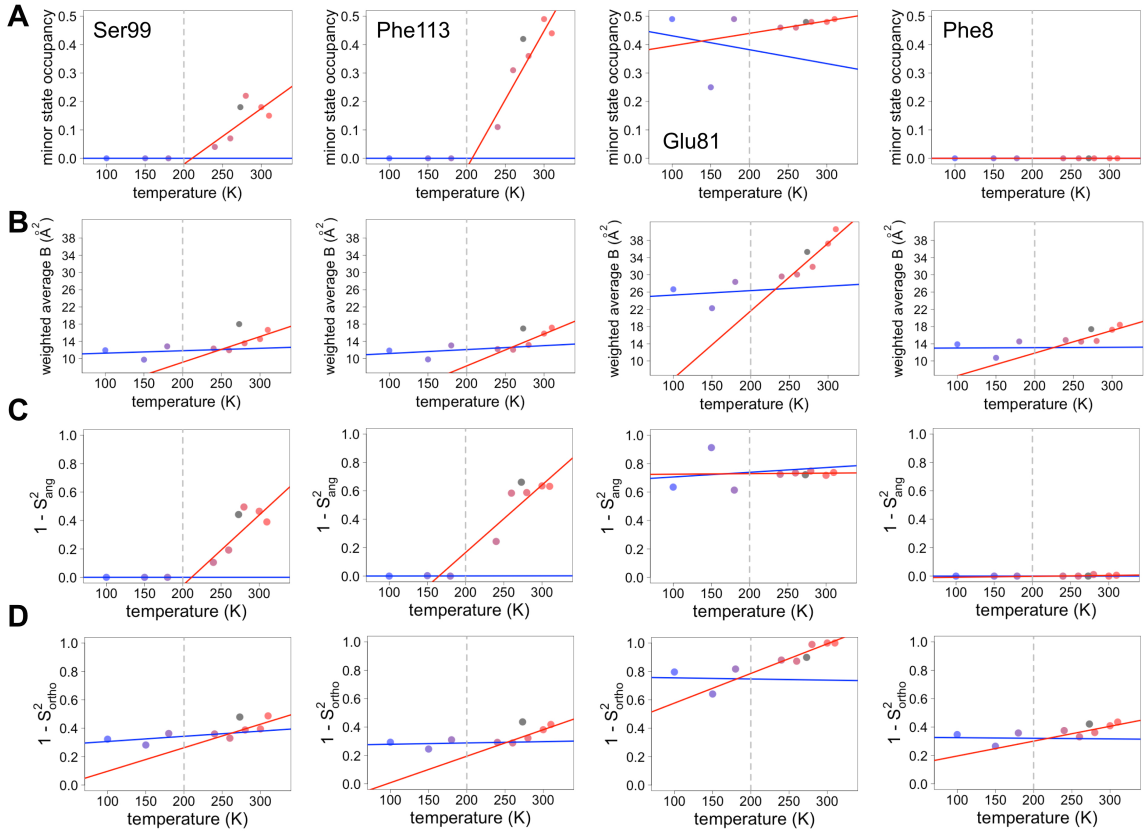

Figure 6 - Figure Supplement 2: Both harmonic and non-harmonic flexibility contribute to changes in order parameters with temperature. (A-D) Contributions to χ1 order parameter vs. temperature for four representative residues in CypA. Ser99 and Phe113 are in the active-site network, Glu81 is surface-exposed and adopts alternative conformations at all temperatures (**Figure 4**), and Phe8 is buried in the protein core and is single-rotamer at all temperatures. Similar conformations within the same rotameric well were grouped together for this analysis. **(A)** Occupancy of minor alternative conformations. **(B)** Intra-residue heavy-atom-average B-factor. **(C)** Complement of the S^2_{ang} component of the χ1 order parameter, which uses occupancy-weighted angles between bond vectors across alternative conformations. **(D)** Complement of the S^2_{ortho} component of the χ1 order parameter, which uses occupancy-weighted B-factors. Placement of XFEL points and coloring as in **Figure 6C,D**.

bioRxiv preprint doi: https://doi.org/10.1101/016733; this version posted March 19, 2015. The copyright holder for this preprint (which was not certified by peer review) is the author/funder, who has granted bioRxiv a license to display the preprint in perpetuity. It is made available under aCC-BY 4.0 International license.

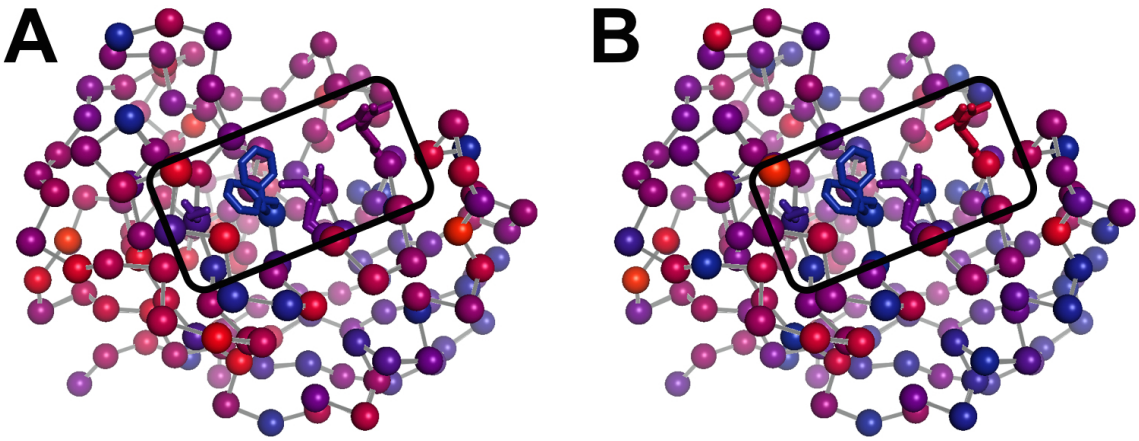

Figure 7: The dynamic transition temperature is variable throughout CypA. Intersection temperatures from **(A)** χ1 order parameters as in **Figure 6B** or **(B)** sidechain terminus order parameters as in **Figure 6 - S1B** are mapped to the 1.2 Å room-temperature synchrotron model. Each residue is marked with a sphere colored based on its apparent transition temperature, from low (blue) to high (red). The active-site network is subdivided: Ser99 and Phe113 (left of boxed region) both transition at a low temperature regardless of order parameter bond vector, but Met61 and Arg55 transition at higher, different temperatures.

bioRxiv preprint doi: https://doi.org/10.1101/016733; this version posted March 19, 2015. The copyright holder for this preprint (which was not certified by peer review) is the author/funder, who has granted bioRxiv a license to display the preprint in perpetuity. It is made available under aCC-BY 4.0 International license.

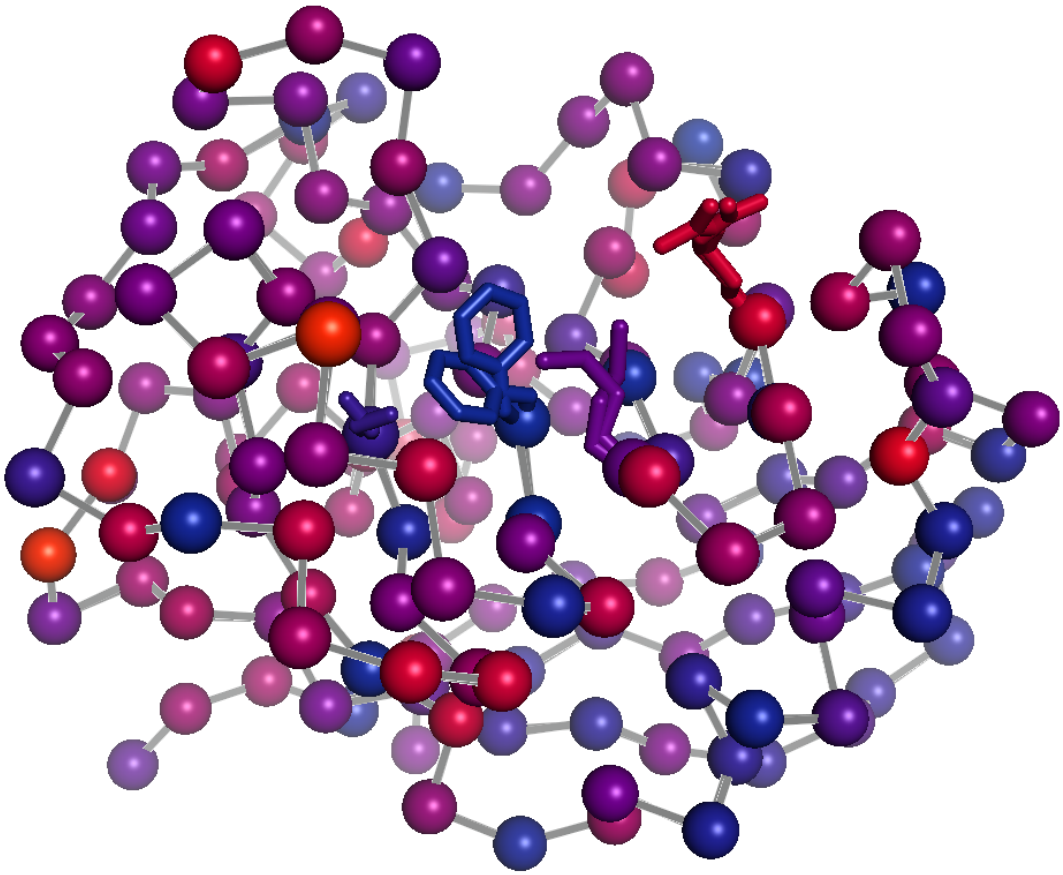

Movie 4: 360˚ rotation around **Figure 7B**.

bioRxiv preprint doi: https://doi.org/10.1101/016733; this version posted March 19, 2015. The copyright holder for this preprint (which was not certified by peer review) is the author/funder, who has granted bioRxiv a license to display the preprint in perpetuity. It is made available under aCC-BY 4.0 International license.

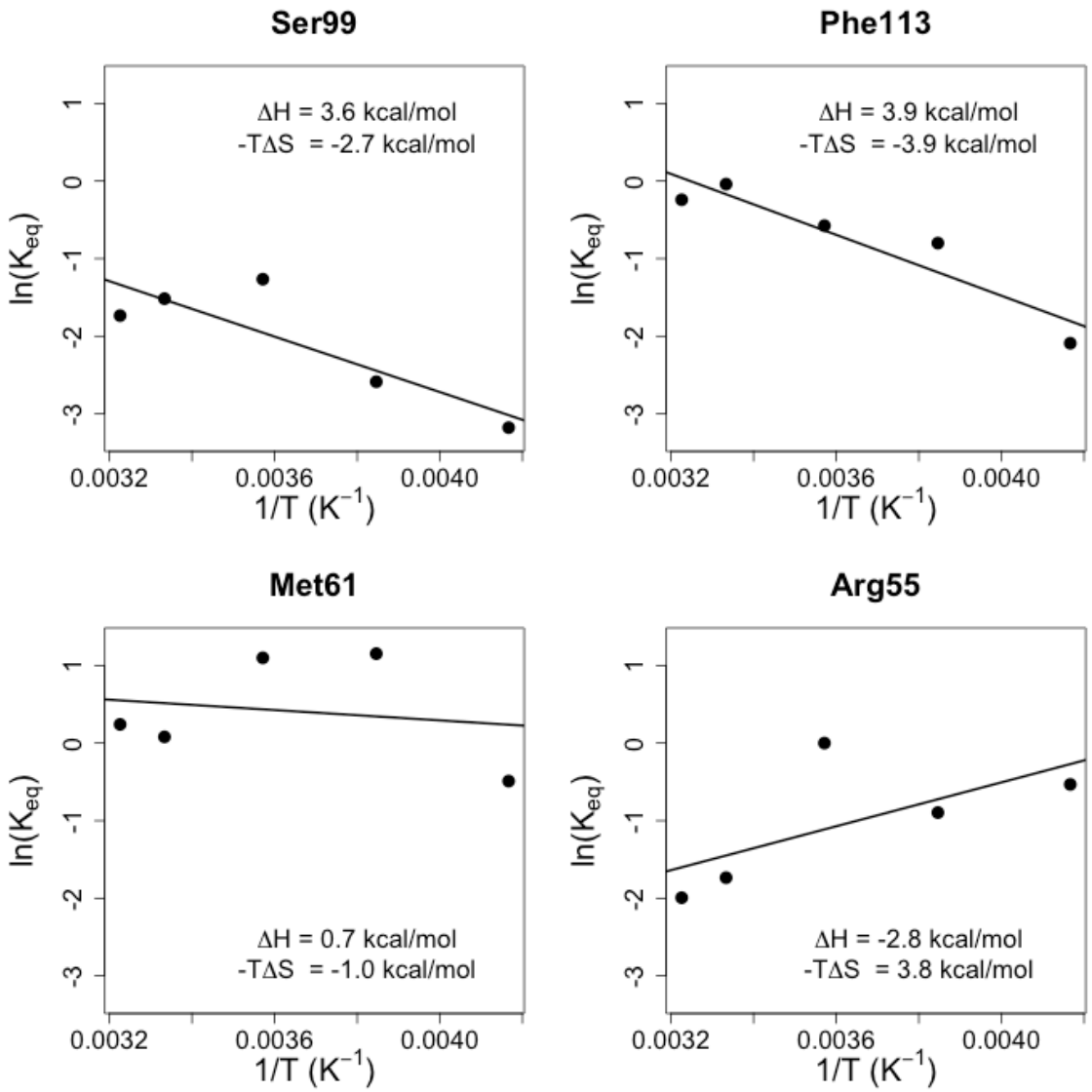

Figure 8: Pseudo Van't Hoff analysis from occupancies of crystallographic alternative conformations. K_{eq} is estimated from the ratio of major- vs. minor-state occupancies. Only the five multitemperature synchrotron models from temperatures above the glass transition (>200 K) were used. Entropies are calculated at approximate physiological temperature (310 K).

bioRxiv preprint doi: https://doi.org/10.1101/016733; this version posted March 19, 2015. The copyright holder for this preprint (which was not certified by peer review) is the author/funder, who has granted bioRxiv a license to display the preprint in perpetuity. It is made available under aCC-BY 4.0 International license.

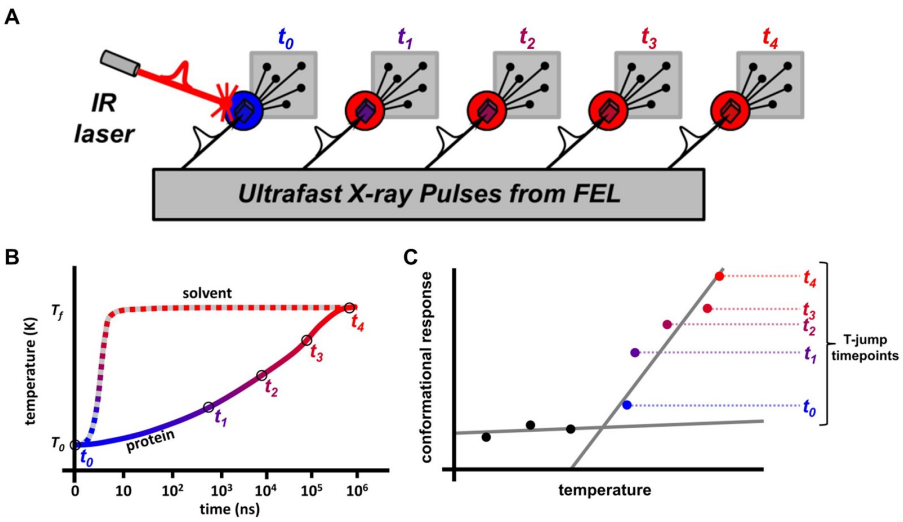

Figure 8 - Figure Supplement 1: Schematic of future XFEL time-resolved experiments to address kinetics. (A) A hypothetical "pump-probe" time-resolved X-ray diffraction experiment to interrogate the kinetics of the conformational transition in the CypA dynamic network. In this experiment, the solvent surrounding and within a CypA crystal can be rapidly heated using a pulsed infrared (IR) laser that is tuned to vibrationally excite water molecules. Following the excitation pulse from the IR laser, the sample can be probed by diffraction from ultrafast X-ray pulses, delivered at precisely timed intervals following IR irradiation (t_0-t_4). **(B)** A schematic of the potential kinetic response to the IR pulse by both solvent and protein. Absorption of the IR pulse will cause the temperature of the solvent to rapidly increase by ~30 K in tens of nanoseconds. While the solvent heats rapidly, the protein will heat more slowly, allowing X-ray diffraction experiments at multiple time points following the temperature-jump. **(C)** A hypothetical plot of protein conformational response as a function of temperature (as in earlier figures) shows the relationship between the present multitemperature study and the future time-resolved, temperature-jump study. Because each conformational degree of freedom can have different kinetic responses to the temperature perturbation, coupling can be determined based on steric considerations and the similarity in response curves.

bioRxiv preprint doi: https://doi.org/10.1101/016733; this version posted March 19, 2015. The copyright holder for this preprint (which was not certified by peer review) is the author/funder, who has granted bioRxiv a license to display the preprint in perpetuity. It is made available under aCC-BY 4.0 International license.

		RT sync	XFEL	100 K	150 K	180 K	240 K	260 K	280 K	300 K	310 K
R_{free} (%)	*raw qFit*	16.7	25.2	19.0	16.9	18.5	17.5	17.9	15.7	16.3	16.1
	final	14.6	24.9	18.3	15.6	17.5	15.6	16.8	14.3	14.4	15.0
	Δ	-2.1	-0.3	-0.7	-1.3	-1.0	-1.9	-1.1	-1.4	-1.9	-1.1
Molprobity score	*raw qFit*	1.47	1.80	1.79	1.31	1.21	1.18	1.45	1.28	0.95	1.19
	final	1.08	1.39	1.19	1.29	0.63	1.14	0.91	1.25	0.99	0.76
	Δ	-0.39	-0.41	-0.80	-0.02	-0.58	-0.04	-0.54	-0.03	+0.04	-0.43

Table 4: Improvements in validation statistics from finalizing raw qFit models. Statistics calculated with *phenix.molprobity*.